Supporting Online Material

for

"Mathematical modeling of planar cell polarity to understand domineering non-autonomy"

Keith Amonlirdviman, Narmada A. Khare, David R.P. Tree, Wei-Shen Chen, Jeffrey D. Axelrod and Claire J. Tomlin

Supporting Text

The Factor X or Z model

To explain how cells mutant for planar cell polarity (PCP) genes can affect the polarity of neighboring, wild-type cells, a class of models has been proposed in which cells respond to an initial cue by producing and secreting a diffusible second factor whose graded distribution determines polarity (*S1–S9*) (Fig. S1). In the eye, Wingless (Wg) signals in a gradient that is highest at the poles and lowest at the equator. It was hypothesized that Wg signaling induces the dose dependent secretion of "factor X," which diffuses, and in turn regulates Frizzled (Fz) signaling (*S2*). Clonal disruption of the response to Wg would perturb the factor X gradient in both the mutant and the neighboring wild-type tissue, thereby producing non-autonomy. Similarly, in response to a graded upstream signal, Fz and Van Gogh (Vang) have been hypothesized to regulate production of a diffusible "factor Z" that is required for polarity readout (*S4, S7*).

Interestingly, while for most *fz* alleles, including null alleles, clones of mutant cells produce domineering non-autonomy, clones of cells mutant for some *fz* alleles produce an almost cell autonomous polarity phenotype (*S10–S12*). Clones of cells mutant for *disheveled* (*dsh*), a component of the Fz signaling pathway (*S13*), also produce nearly cell autonomous polarity disruptions (*S14, S15*). Diffusible factor models explain these observations with the hypothesis that Fz mediates two separately mutable signaling functions, transducing a cell autonomous signal through Dsh, and a Dsh independent non-autonomous signal (*S16–S19*). The non-autonomous signal was proposed to be mediated by factor X, or a second, similar, factor Z, in this case produced in response to Fz signaling, and feeding back through

Fz, while the autonomous signal was proposed to initiate cell polarization (*S4, S7*). Non-autonomous Fz signaling has been proposed to temporally precede autonomous signaling in both the eye and wing (*S19*). However, despite the ability of these models to explain domineering non-autonomy, diffusible factors X or Z have not been identified (*S6*), and no molecular level understanding of the autonomous and non-autonomous signaling functions of Fz has been obtained (*S7, S19*).

Mathematical model formulation

The mathematical model of PCP signaling represents a network of the four proteins, Dsh, Fz, Prickle-spiny-legs (Pk) and Vang. The essential logic of this feedback loop is preserved by representing these interactions as binding to form protein complexes (Fig. 1D of the main text). For example, Fz interacts with Dsh to form a DshFz complex, and Vang interacts with Pk to form VangPk. For the reaction between cells, Fz on the membrane of one cell reacts with Vang on the membrane of a neighboring cell to form a complex denoted FzVang. FzVang is then restricted to diffusing only along the shared edge of the cells. FzVang can further react with Dsh or Pk to form larger complexes. Backward reactions separate the complexes back into their constituent proteins. The six protein complexes included in this model are DshFz, VangPk, FzVang, DshFzVang, FzVangPk and DshFzVangPk. The last four of these complexes are formed across the cell membranes of adjacent cells. It is assumed that protein concentrations may be treated as continuously varying sample averages. Dsh and Pk are assumed to diffuse freely and isotropically within the cell interior. Vang, Fz and the complexes diffuse only in the membrane. The four complexes that form between adjacent

cells are restricted to diffuse in the cell edge common to the cells involved in the formation of the complex. The geometry of the physical cell network develops into a close-packed planar arrangement of hexagonal cells. In order to simplify the numerical computations, the geometry is assumed to remain fixed throughout the signaling and protein localization process.

The model is represented by the following ten reactions occurring at the cell edges.

$$\mathrm{Dsh} + \mathrm{Fz} \underset{A_1 B \lambda_1}{\overset{R_1}{\rightleftarrows}} \mathrm{DshFz} \tag{S1}$$

$$\mathrm{Fz}^{\dagger} + \mathrm{Vang} \underset{\lambda_2}{\overset{R_2}{\rightleftarrows}} \mathrm{FzVang} \tag{S2}$$

$$\mathrm{Vang} + \mathrm{Pk} \underset{\lambda_3}{\overset{R_3}{\rightleftarrows}} \mathrm{VangPk} \tag{S3}$$

$$\mathrm{DshFz}^{\dagger} + \mathrm{Vang} \underset{\lambda_4}{\overset{R_4}{\rightleftarrows}} \mathrm{DshFzVang} \tag{S4}$$

$$\mathrm{Dsh}^{\dagger} + \mathrm{FzVang} \underset{A_1^{\dagger} B^{\dagger} \lambda_5}{\overset{R_5}{\rightleftarrows}} \mathrm{DshFzVang} \tag{S5}$$

$$\mathrm{Fz}^{\dagger} + \mathrm{VangPk} \underset{\lambda_6}{\overset{R_6}{\rightleftarrows}} \mathrm{FzVangPk} \tag{S6}$$

$$\mathrm{FzVang} + \mathrm{Pk} \underset{\lambda_7}{\overset{R_7}{\rightleftarrows}} \mathrm{FzVangPk} \tag{S7}$$

$$\mathrm{Dsh}^{\dagger} + \mathrm{FzVangPk} \underset{A_1^{\dagger} B^{\dagger} \lambda_8}{\overset{R_8}{\rightleftarrows}} \mathrm{DshFzVangPk} \tag{S8}$$

$$\mathrm{DshFz}^{\dagger} + \mathrm{VangPk} \underset{\lambda_9}{\overset{R_9}{\rightleftarrows}} \mathrm{DshFzVangPk} \tag{S9}$$

$$\mathrm{DshFzVang} + \mathrm{Pk} \underset{\lambda_{10}}{\overset{R_{10}}{\rightleftarrows}} \mathrm{DshFzVangPk} \tag{S10}$$

where the reaction-based global biasing signal is introduced through

$$A_1 = \begin{cases} M_1, & \text{Distal region of the cell} \\ 1, & \text{Otherwise} \end{cases}$$

and Pk and Vang inhibition is introduced through

$$B = 1 + K_b(K_{\text{Pk}}[\text{Pk}] + [\text{VangPk}] + [\text{FzVangPk}] + [\text{DshFzVangPk}] + K_{\text{Vang}}([\text{Vang}] + [\text{FzVang}] + [\text{DshFzVang}]))^{K_p}$$

R_1 through R_{10} are forward reaction rate constants. λ_1 through λ_{10} are backward reaction rate constants. The effect of Pk and Vang inhibiting the recruitment of Dsh to the membrane is modeled in Eqs. S1, S5 and S8 as a promotion in the backward reaction rates in proportion to the local concentration of Pk and Vang raised to the exponent K_p, with constant of proportionality K_b. K_{Pk} is a constant that multiplies only the concentration of unbound Pk, and likewise K_{Vang} is a constant that multiplies only the concentration of Vang not bound to Pk. K_{Pk} and K_{Vang} may be set to 0 if only the complexes containing VangPk should have an inhibitory effect. K_{Pk} and K_{Vang} were set to 0.5, so that Vang and Pk had equal and additive inhibitory effects. K_p is used to approximate non-linearity in the inhibitory effects of Pk and Vang. The daggered (†) variables indicate that the reaction occurs with the protein across the cell membrane in a neighboring cell. For convenience, we have arbitrarily chosen in our notation to associate the complexes spanning multiple cells with the source cell for Vang. The backward reaction of Eqs. S2, S4-S6, S8 and S9 locate the products in their original cells so that the total amount of each protein in a cell is always conserved.

The mechanism by which the global Ft signal influences the feedback loop is not yet understood. Two possible mechanisms that we have explored are 1) an asymmetry in the rate at which Dsh and Fz interact, such that in a region of the distal edge of each cell, λ_1, λ_5 and λ_8 are multiplied by $M_1 < 1$ and 2) an asymmetry in the fraction of Fz and Fz containing complexes that is diffusible, such that in a region of the distal edge of each cell the concentrations of Fz and Fz complexes are multiplied by $M_2 < 1$.

The net local forward reaction rates implied by Eqs. S1-S10 are denoted by P_1 through P_{10}. They represent the difference of the forward and backward reactions, given by

$$P_1 = R_1[\text{Dsh}][\text{Fz}] - A_1 B \lambda_1[\text{DshFz}] \tag{S11}$$

$$P_2 = R_2[\text{Fz}]^\dagger[\text{Vang}] - \lambda_2[\text{FzVang}] \tag{S12}$$

$$P_3 = R_3[\text{Vang}][\text{Pk}] - \lambda_3[\text{VangPk}] \tag{S13}$$

$$P_4 = R_4[\text{DshFz}]^\dagger[\text{Vang}] - \lambda_4[\text{DshFzVang}] \tag{S14}$$

$$P_5 = R_5[\text{Dsh}]^\dagger[\text{FzVang}] - A_1^\dagger B^\dagger \lambda_5[\text{DshFzVang}] \tag{S15}$$

$$P_6 = R_6[\text{Fz}]^\dagger[\text{VangPk}] - \lambda_6[\text{FzVangPk}] \tag{S16}$$

$$P_7 = R_7[\text{FzVang}][\text{Pk}] - \lambda_7[\text{FzVangPk}] \tag{S17}$$

$$P_8 = R_8[\text{Dsh}]^\dagger[\text{FzVangPk}] - A_1^\dagger B^\dagger \lambda_8[\text{DshFzVangPk}] \tag{S18}$$

$$P_9 = R_9[\text{DshFz}]^\dagger[\text{VangPk}] - \lambda_9[\text{DshFzVangPk}] \tag{S19}$$

$$P_{10} = R_{10}[\text{DshFzVang}][\text{Pk}] - \lambda_{10}[\text{DshFzVangPk}] \tag{S20}$$

P_1 through P_{10}, along with the protein and complex concentrations, are continuous functions of both position and time.

The complete set of partial differential equations (PDEs) that serve as the governing equations for the mathematical model are then obtained by adding the above reaction terms with the appropriate diffusion terms to determine the time rate of change for each of the protein and complex concentrations. We make the further simplification, by taking advantage of the planar nature of this cell network, of modeling the cell locations in only two-dimensions. The resulting system of PDEs is

$$\frac{\partial[\mathrm{Dsh}]}{\partial t} = -P_1 - P_5^{\dagger} - P_8^{\dagger} + \mu_{\mathrm{Dsh}}\nabla^2[\mathrm{Dsh}] \tag{S21}$$

$$\frac{\partial[\mathrm{Pk}]}{\partial t} = -P_3 - P_7 - P_{10} + \mu_{\mathrm{Pk}}\nabla^2[\mathrm{Pk}] \tag{S22}$$

$$\frac{\partial[\mathrm{Fz}]}{\partial t} = -P_1 - P_2^{\dagger} - P_6^{\dagger} + \mu_{\mathrm{Fz}}\nabla^2[\mathrm{Fz}]_D \tag{S23}$$

$$\frac{\partial[\mathrm{Vang}]}{\partial t} = -P_2 - P_3 - P_4 + \mu_{\mathrm{Vang}}\nabla^2[\mathrm{Vang}] \tag{S24}$$

$$\frac{\partial[\mathrm{DshFz}]}{\partial t} = P_1 - P_4^{\dagger} - P_9^{\dagger} + \mu_{\mathrm{DshFz}}\nabla^2[\mathrm{DshFz}]_D \tag{S25}$$

$$\frac{\partial[\mathrm{VangPk}]}{\partial t} = P_3 - P_6 - P_9 + \mu_{\mathrm{VangPk}}\nabla^2[\mathrm{VangPk}] \tag{S26}$$

$$\frac{\partial[\mathrm{FzVang}]}{\partial t} = P_2 - P_5 - P_7 + \mu_{\mathrm{FzVang}}\nabla_s^2[\mathrm{FzVang}]_D \tag{S27}$$

$$\frac{\partial[\mathrm{DshFzVang}]}{\partial t} = P_4 + P_5 - P_{10} + \mu_{\mathrm{DshFzVang}}\nabla_s^2[\mathrm{DshFzVang}]_D \tag{S28}$$

$$\frac{\partial[\mathrm{FzVangPk}]}{\partial t} = P_6 + P_7 - P_8 + \mu_{\mathrm{FzVangPk}}\nabla_s^2[\mathrm{FzVangPk}]_D \tag{S29}$$

$$\frac{\partial[\mathrm{DshFzVangPk}]}{\partial t} = P_8 + P_9 + P_{10} + \mu_{\mathrm{DshFzVangPk}}\nabla_s^2[\mathrm{DshFzVangPk}]_D \tag{S30}$$

where μ_{Dsh}, μ_{Pk}, μ_{Fz}, μ_{Vang}, μ_{DshFz}, μ_{VangPk}, μ_{FzVang}, $\mu_{\mathrm{DshFzVang}}$, μ_{FzVangPk} and $\mu_{\mathrm{DshFzVangPk}}$ are diffusion rate constants and where the diffusion-based global biasing signal is introduced by multiplying the concentrations of those terms with the D subscript by a factor of $M_2 < 1$ in the distal region of the cell. The subscript s for the Laplacian in Eqs. S27-S30 indicates

that the operator is applied only within shared cell edges between two cells.

In Fig. S11 we show a simulation using a Fz variant, denoted $Fz^{autonomous}$, in which the interactions between Dsh and Fz have been reduced, in a wild-type background. For this simulation, an expanded set of equations was used so that both Fz and $Fz^{autonomous}$ could be considered in the same simulation. Every equation and complex involving Fz was replicated with a corresponding equation involving $Fz^{autonomous}$ with the same rate constant values except for those affecting the interaction between Dsh and $Fz^{autonomous}$. This resulted in a system of 16 PDEs that were discretized and simulated in the same fashion as the original equations.

Numerical methods

Eqs. S21-S30 were discretized using standard finite volume methods, in which the spatial variable values are taken to represent averages over a finite number of control volumes. This formulation is well suited for modeling conserved quantities in irregular computational grid geometries and can be exploited to handle unstructured, arbitrary meshes so that this model can be extended to accept actual cell geometries. The resulting system was numerically integrated using a semi-implicit Euler method with a variable time step in order to balance numerical stability and accuracy with computational efficiency (*S20*).

The geometry of the cells is illustrated in Fig. S2. The space illustrated between the cells is meant only to indicate that the walls of distinct cells are represented separately in the computational model, even though they are treated as occupying the same spatial location. Each cell was further discretized into a triangular mesh. The coarseness of the

mesh could be selected, depending on the degree of accuracy or computational efficiency required.

Within each cell, homogeneous Neumann boundary conditions were applied for [Dsh] and [Pk]. The membrane-bound proteins and complexes have either periodic boundary conditions applied, for those that are allowed to diffuse completely around the membrane, or homogeneous Neumann boundary conditions, for those restricted to the cell wall shared between two adjacent cells (*S20*).

Periodic boundary conditions were used for the intercellular signaling terms, such that each cell was effectively surrounded by an infinite array of cells. When simulating patches of mutant cell clones, we chose the sizes of the cell networks so that they were large enough for variations in localization patterns between cells to decay before reaching the edge of the simulated array in order to prevent these variations from interfering with each other. We also implemented a reflection plane boundary condition parallel to the proximal-distal axis, so that the size of the computational domain could be effectively doubled for symmetric cases.

Given limited computational resources and the large number of simulation cases necessary, particularly during parameter selection, we chose relatively coarse grids on which to perform our simulations. While grid refinement showed variation in the numerical results, the qualitative features of the simulation results remained the same. Because our goal was to demonstrate the ability of some reasonable abstraction of the biological model to reproduce specified phenotypes, numerical errors arising from the coarseness of the discretization did not substantially alter our results.

The hair growth direction for each simulated cell is determined based on the protein concentration distribution at the end of the simulation. Although the mechanism for how the protein distribution is translated into a location for hair initiation is not known, we chose to use the distribution of Dsh to predict the hair growth direction because we observe that hairs emerge consistently from the center of the cell in *dsh* mutants but not in the other mutants (Fig. S3). Therefore, the hair growth direction predicted by this model is calculated as the direction corresponding to the vector sum of Dsh localization in each cell. If the Dsh concentration is not polarized above a specified threshold, then the hair is assigned to the center of the cell.

Parameter selection

The unspecified model parameters were the initial concentrations for each of the proteins (denoted $[\mathrm{Fz}]_0$, $[\mathrm{Pk}]_0$, $[\mathrm{Vang}]_0$ and $[\mathrm{Dsh}]_0$), the diffusion constants for each of the proteins and protein complexes, R_1 through R_{10}, λ_1 through λ_{10}, K_b, K_p, M_1 and M_2. The unit of measure for concentration in the problem was unspecified, so we reduced the number of parameters by arbitrarily fixing the initial Dsh concentration, $[\mathrm{Dsh}]_0$, to 1. We identified these parameters by constraining them so that the simulation would reproduce qualitative features of the experimentally observed PCP phenotypes. For example, one case involved simulating clones of cells lacking *fz* function surrounded by wild-type cells, and constraining the parameters so that at the end of the simulation, the hair polarity was reversed in a wild-type cell that was distal to the mutant cells. The degree of asymmetry was scored in this cell based on the asymmetric distribution of the Dsh concentration at the end of a

simulation for a given set of parameters, and the constraint was implemented as a quadratic penalty function that was non-zero when the polarity in this cell was not reversed above a threshold target value. An objective function, J, was constructed by summing similarly constructed penalty constraint functions for each of the feature constraints corresponding to the characteristic PCP phenotypes listed in Table S1. Consequently, each objective function evaluation involved running several simulations corresponding to each of the different cases. In order to reduce the amount of computational effort required for each objective function evaluation, cases involving mutant clones were simulated on lines of wild-type cells extending parallel to the proximal-distal axis and interrupted by mutant cells. Due to the periodic boundary conditions, these cases effectively simulated repeating infinite lines of mutant cells extending parallel to the anterior-posterior axis in an infinite array of wild-type cells. Once parameters were identified that satisfied the constraints on the simpler lines of cells, we verified that they continued to exhibit the desired behavior on the larger two-dimensional arrays shown in the results. Additional objective terms were also added to J to favor the accumulation of proteins on the proximal-distal membranes instead of the anterior-posterior membranes in the wild-type case.

In order to replicate the phenotypes involving the overexpression of *pk*, an additional parameter, M_o, representing the factor by which proteins are overexpressed above wild-type levels in cases involving overexpression mutants, was also included as a parameter to be identified. If M_o were too close to 1, then clones of cells overexpressing *pk* would appear as wild-type cells and the domineering non-autonomy proximal to such clones would not be observed. Our model does not allow for the inhibitory effect of high Pk concentrations to

saturate, and so extremely large concentrations of Pk would completely inhibit the ability of Dsh to interact with Fz, disrupting Dsh accumulation at the membrane. However, large regions of *pk* overexpression have been observed to instead maintain, and perhaps even to promote the recruitment of Dsh to the membrane (*S21*). Therefore, we wish to show that for some set of parameters, increasing the Pk concentration acts to enhance the feedback loop. Indeed, our model predicts some finite range for M_o over which the experimentally observed phenotypes are reproduced. In reality, the ability of Pk to inhibit the interaction between Dsh and Fz may saturate or behave in a more complex fashion than is modeled here, possibly allowing for a larger range for M_o that reproduces the observed phenotypes.

The model parameters were determined by applying the Nelder-Mead simplex method (*S22*) to the non-linear optimization problem

$$\begin{aligned}
&\text{Minimize} && J \\
&\text{Subject to} && K_b,\ K_p \geq 0 \\
& && R_1,\ R_2,\ R_3,\ R_4,\ R_5,\ R_6,\ R_7,\ R_8,\ R_9,\ R_{10} \geq 0 \\
& && \lambda_1,\ \lambda_2,\ \lambda_3,\ \lambda_4,\ \lambda_5,\ \lambda_6,\ \lambda_7,\ \lambda_8,\ \lambda_9,\ \lambda_{10} \geq 0 \\
& && M_1 < 1 \text{ or } M_2 < 1 \\
& && M_o > 1 \\
& && \mu_{\text{Dsh}},\ \mu_{\text{Pk}},\ \mu_{\text{Fz}},\ \mu_{\text{Vang}},\ \mu_{\text{DshFz}} \geq 0 \\
& && \mu_{\text{VangPk}},\ \mu_{\text{FzVang}},\ \mu_{\text{DshFzVang}},\ \mu_{\text{FzVangPk}},\ \mu_{\text{DshFzVangPk}} \geq 0 \\
& && [\text{Dsh}]_0 = 1,\ [\text{Fz}]_0,\ [\text{Pk}]_0,\ [\text{Vang}]_0 > 0
\end{aligned}$$

The search space for the model rate parameters and the various multiplicative factors spanned several orders of magnitude, and so the optimization was performed on the loga-

rithm of these parameters. The parameters were selected by iteratively running the optimization routine after adjusting the weights and the steepness of the penalty functions for each of the individual feature constraints.

Parameter sensitivity analysis

Once parameter sets were determined that simultaneously satisfied all of the feature constraints, we determined ranges in which each of the parameters could vary, while keeping all other parameters fixed, and still satisfy each of the feature constraints (Fig. S4). A caveat to these data is that the feature constraints are defined on only some cells in each case, and that the constraints are enforced only on the simplified linear cell arrays as described above. Therefore, satisfaction of these feature constraints does not guarantee that all of the cells in a two-dimensional array would qualitatively match experimental observations. Furthermore, these ranges do not necessarily imply any relationships between the relative values of different parameters, because only one parameter was permitted to vary at a time. We did not intend for these constraints to completely determine whether a set of simulation results rigorously satisfied the qualitative observations that have been made in various PCP experiments, and we believe that attempting to identify such constraint functions would be misleading. In particular, the behaviors of some mutant phenotypes do not occur with the same regularity as the wild-type phenotype and may vary somewhat in repeated experiments. Rather than finding exact parameters ranges, our intent here is instead to give some reasonable indication of the sensitivity of our model to the model parameters, and to gain some additional insight into the role that various model components play in determining

the dynamics of this system. Finally, these parameters were varied for every cell in the network simultaneously. Therefore, these ranges should not be considered ranges in which the parameters of every cell in the network must lie, but rather average or nominal parameter values for most of the cells in a network. Indeed, we have shown in simulations in which we disrupted the input asymmetry signal in a small patch of cells within a network of wild-type cells, that all of the cells maintain the wild-type hair polarity despite the presence of cells that behave according to parameter values outside of the ranges that we have found here.

These results show that the selected parameter set is not unique, nor necessarily the correct set of parameters satisfying the feature constraints. Instead, a wide range of parameters are possible, and so the identification of a model rate parameter that is different than the precise values used in our simulation would not immediately invalidate the conclusions that we draw regarding the feasibility of our model.

Assumptions and limitations

Reactions are deterministic

We have assumed that conditions are met such that protein concentrations may be treated as continuous, deterministic variables. The discrepancy between deterministic models and stochastic models of these reactions increases when the number of reacting molecules is small, the reactions proceed very slowly or if the behavior of the signaling network depends on the random fluctuations in protein concentrations, rather than on their average values (*S23–S26*). The biological model does not rely on fluctuations of protein concentrations, and the time scale for the asymmetric accumulation of Fz, Dsh, Pk and Vang is much

greater than the time necessary for protein-protein interactions. Furthermore, the minimal level of detection of fluorescently tagged molecules, localized to the plasma membrane, used to visualize these proteins suggests that the number of molecules present in each cell is likely to be on the order of thousands or more (*S27*). Therefore, we would not expect that the increased computational effort of stochastic models would be necessary, and indeed, we have shown that a deterministic model is sufficient to reproduce the behavior of the system.

The cell network geometry is modeled by a two-dimensional, fixed, regular, hexagonal array

The planar nature of the signaling network allows us to mathematically model the logic of the biological feedback loop model in two-dimensions, and so for simplicity, we have disregarded the depth of the cells. The computational grid geometry describes a regular hexagonal array of cells (Fig. S2) that remains fixed throughout the simulation. *Drosophila* wing epithelial cells are generally hexagonally packed, but the precise size and shape of the cells vary over the wing and during PCP signaling. These geometric variations likely influence precise hair angles, the degree of asymmetric localization of proteins, and the extent of non-autonomous polarity disruptions in regions near some mutant clones. The mathematical model only attempts to reproduce general qualitative features of PCP phenotypes, and so these variations are not considered in the current model.

Protein and complex movements are modeled by diffusion

The movement of proteins and complexes within each cell has been modeled as diffusion, though more complex mechanisms may be involved. We found that the results were not

very sensitive to diffusion rate parameters, permitting us to perform many of our computations on very coarse grids while still reproducing the behavior of the system. Since diffusion does not favor asymmetric distributions, should a more complex mechanism for component movement be discovered, such as active transport, the model should easily accommodate this and achieve equally good or better results.

The feedback loop is modeled by complex formation

While the underlying mechanisms for the interactions in the local feedback loop are not yet fully understood, the essential logic of this feedback loop is preserved by representing these interactions as binding to form protein complexes (Fig. 1D of the main text). Direct biochemical evidence exists for the VangPk complex (*S28, S29*). It has been observed that Fz induces the recruitment of Dsh to the cell membrane in vivo and in heterologous systems, and evidence of direct, albeit weak, binding exists for Fz and the PDZ domain of Dsh (*S30, S31*). Whether these proteins directly interact, or if they interact through one or a series of intermediary proteins is not expected to alter the nature of the results of this model.

We modeled a direct Fz-Vang interaction, though this has not been demonstrated. Fz and Vang localize to opposite sides of the cell, and we have shown that Vang accumulation depends on the Fz allele (autonomous or non-autonomous) in the adjacent cell. However, a direct interaction need not be invoked to preserve the logic of our model. For example, Fz and Vang could be linked through a mutual affinity for a bridging cadherin such as Flamingo (Fmi), which is most likely present in both membranes, and is required for assembly of the

other components (*S32*).

Fmi (*S18, S32*), Diego (Dgo) (*S33, S34*) and Widerborst (Wdb) (*S35*), other proteins known to be involved in PCP signaling, were not included in the model, as their roles are insufficiently understood. Fmi is required for the membrane localization of the other proteins (*S28*), Dgo localizes to the proximal cell surface (*S34*), and both are required to generate asymmetry, but otherwise, it is unknown how Fmi and Dgo influence other proteins. When the role of these proteins is more fully understood, they may be included in the model without perturbing the function of the feedback loop, and could provide additional degrees of freedom that may enhance the concordance with experimental data. Therefore, the feasibility of our model should not be sensitive to these assumptions.

Pk and Vang inhibit the Dsh-Fz interaction

Both genetic and cell culture data previously led us to propose that Pk inhibits Fz dependent membrane recruitment of Dsh (*S21*). In a cell culture assay, we showed that Pk cell-autonomously antagonizes Dsh recruitment (*S21*). This result has been replicated by some, but not others (*S28, S36–S38*). In new experimental results, we have demonstrated a dose dependent inhibition of Dsh membrane recruitment by both Pk and Vang, and a combinatorial effect when both are expressed (Fig. S5). This is consistent with the hypothesis that Pk and Vang work together on the proximal side of the cell, and with the observation that, like Pk, Vang binds Dsh (*S21, S28, S39*). The differences between our results and those of others might therefore depend on differences in the uncontrolled levels of host cell Vang, or other uncontrolled aspects of the experiment. We do not know the mechanism by

which Pk and Vang antagonize DshFz complex formation, but we do not see colocalization of Dsh with Pk and Vang at the end of PCP signaling, suggesting that Dsh does not remain bound to Pk and Vang after this inhibition has taken place. Therefore, we expect that the mechanism for this inhibition is more complicated than competitive binding, such as some modification that then destabilizes the FzDsh complex. The implementation of Pk and Vang inhibition used in the mathematical model only requires that these proteins inhibit the Dsh-Fz interaction, without relying on a specific molecular mechanism for this activity.

The form of the direct, global asymmetry signal is not fully understood

Several possible mechanisms exist for providing the asymmetric signal that the Fz feedback loop interprets, and then uses to produce, from an initially symmetric distribution, the asymmetric localization of the proteins included in the model (Fz, Dsh, Vang and Pk). In the first possibility, the Fz feedback loop responds to a signal whose concentration or activity is already asymmetric within each cell, resulting in an asymmetric response that is similar throughout the wing (Fig. S6A). For example, Wdb is asymmetrically arrayed in cells preceding the observed asymmetry of Fz, Dsh, Vang and Pk; its function is required for asymmetry of Fz, Dsh, Vang and Pk, but not vice versa (*S35*). This is the mechanism used for the two forms of the asymmetry signal implemented in the mathematical model, and we favor this model because of the existing biological evidence for Wdb asymmetry.

In a second possible mechanism, the asymmetry signal could be an expression gradient producing a response that is uniform within each cell but that varies from cell to cell (Fig. S6B). In this mechanism, it is the difference in the relative response of each cell

compared to its neighbors that serves to bias the network in a particular direction. The periodic boundary conditions implemented in the model prevent us from representing a monotonically increasing response of the network within a cell array of a computationally tractable size. However, we argue that the differences in the relative concentrations of proteins and complexes in neighboring cells would result in an asymmetry in the reaction rates between the proximal and distal edges of a cell. Therefore, we do not expect that the form of this asymmetry would be very different from the form that we have implemented in the reaction-based asymmetry signal, and so we believe that similar results could also be obtained if this form of the asymmetry signal were implemented.

In a third possible mechanism, the network responds directly to a globally imposed gradient, resulting in a network response that is both asymmetric within each cell and different from neighboring cells (Fig. S6C). Such a signal can be decomposed into an asymmetry signal resulting from differences between the response of neighboring cells (as in Fig. S6B) and the asymmetric response within each cell. We wished to ask if our results were also consistent with an asymmetry signal that resulted from this second component, in which the directional bias does not depend on interactions with neighboring cells, but where the input asymmetry signal could vary globally. Assuming that the global gradient is shallow, the input asymmetry signal might appear to be slowly varying within small regions of cells, but vary greatly over the entire wing (Fig. S6D). All of the cells in the proximal region of the global gradient may respond similarly to the asymmetry signal, while cells in a distal region of the global gradient may respond quite differently. If the reduction in the terms modified by the reaction-based direct asymmetry signal, λ_1, λ_5 and λ_8, on the distal boundary of a

cell is to represent a direct reading of a global gradient, then these values should take on a much lower value in the distal region of the wing than in the proximal region. Therefore, we sought to find a set of parameters for which an order of magnitude reduction in λ_1, λ_5 and λ_8 would produce qualitatively similar results. Fig. S4I indicates that the feature constraint corresponding to the overexpression of Vang was the only one that would show an observable change in behavior when λ_1, λ_5 and λ_8 were decreased by an order of magnitude, because both λ_1 and λ_5 lie near the edges of their permitted ranges. From this observation, we were able to select a new parameter set in which we increased λ_1 by an order of magnitude to represent cells in the proximal region of the wing. Results from this parameter set (not shown) satisfied all of the feature constraints, and appeared similar to the results presented in Figs. S7-S10. Then, when λ_1, λ_5 and λ_8 were simultaneously decreased by an order of magnitude to represent cells in the distal region of the wing, the results appeared essentially unchanged (not shown), suggesting that our conclusions regarding the feasibility of the model are also consistent with a direct reading of a gradient to produce an input asymmetry signal within each cell (Fig. S6D).

We have attempted to address the lack of specific knowledge as to how the asymmetry signal influences the feedback loop by showing that the model is not very sensitive to the implementation or the magnitude of the input asymmetry. We implemented two forms of a direct biasing signal (Fig. S6A), one influencing reaction rates, using the term M_1, and another influencing diffusion terms, using the term M_2, and found that both models produced essentially similar results (cf. Figs. 2 of the main text and S7-S10 with Figs. S12-S16). We also tested the requirement for persistence and uniformity of the asymmetry signal. Results

from numerical simulations in which we removed the asymmetry signal in small patches of cells show normal polarity, indicating that the asymmetry signal need not be present or identical in every cell in order to produce the correct wild-type polarity. Simulations in which we removed the asymmetry half of the way through the simulation or in which no asymmetry signal was present during the first quarter of the simulation also show correct polarity, indicating that the results are not highly sensitive to temporal disturbances in the asymmetry signal. Indeed, once some asymmetry had been introduced into network, the feedback loop was observed to continue to amplify this asymmetry in simulation even once the external asymmetry signal had been removed. Therefore, we would expect that any reasonable mechanism for breaking the symmetry in the system would work, and so the conclusions we draw with respect to autonomy do not depend on a specific mechanism for the asymmetry signal. It is not yet apparent whether this type of modeling can predict any differences between the different mechanisms that may be observed experimentally.

Quantitative predictions depend on the choice of parameters

The lack of a detailed biological understanding limits the ability of the mathematical model to make quantitative predictions about the detailed behavior of PCP signaling. We have only enforced qualitative feature constraints during parameter selection, and so quantitative results from the model, such as the degree of asymmetry observed in each of the proteins or the extent of non-autonomy observed around mutant clones, could vary with the specific choice of parameters without violating the feature constraints. Further, the feature constraints were enforced only based on features of the results at the end of each simulation.

Therefore, the dynamic behavior of the model, which also depends on the choice of parameters, does not necessarily reflect the behavior of the biological system. Finally, the relative values and stabilities of the model parameters are themselves dependent on the choice of the other parameters in the model. A different choice of parameters might exhibit different relative parameter values or stabilities, and so we have refrained from making any inferences about the relative importance of various parameters based on the current parameter set.

Relative activity and concentrations of $\mathrm{Fz}^{\mathrm{autonomous}}$ *are unknown*

We hypothesized that $\mathrm{Fz}^{\mathrm{autonomous}}$ should be deficient in its ability to interact with Dsh. The specific degree of reduction in this activity level was chosen arbitrarily between 0% and 0.02% to demonstrate the effect of reducing the interaction of Fz with Dsh, while keeping the interaction with Vang intact.

In Fig. S11 $\mathrm{Fz}^{\mathrm{autonomous}}$ is present in a wild-type background at a concentration of 10% that of Fz. This value was chosen because in the experiment in question, it was noted that only weak apical expression of the protein was seen (*S40*). A similar simulation, modeling $\mathrm{Fz}^{\mathrm{autonomous}}$ at 100% of the Fz concentration also shows that the $\mathrm{Fz}^{\mathrm{autonomous}}$ is nearly symmetrically distributed relative to the asymmetric distribution of Fz (as in the 10% case), but the degree of asymmetry observed in Fz was also reduced (not shown).

Rationalization of phenotypes

Simulations of cells overexpressing *pk* offer some insight into why Dsh and Fz can continue to accumulate asymmetrically at the cell membrane despite the increased presence of a factor

inhibiting their interaction (Figs. 3 of the main text, S10 and S16). Upon *pk* overexpression, an increased Pk concentration is also available to complex with proteins in neighboring cells, reinforcing the feedback loop to produce a greater asymmetric localization of all of the proteins, and consequently offsetting the reduced interaction between Dsh and Fz that would be expected in isolated cells where the feedback loop could not function. We note that simulation of sufficiently high levels of Pk can block most Dsh membrane association and prevent asymmetry, assuming a non-saturable inhibition (not shown).

Consistent with the choice of the Dsh distribution as the basis for predicting hair directions, in simulation, the removal of Dsh from all cells results in the loss of polarity (not shown). Similarly, the removal of Fz from all cells in simulation prevents the membrane recruitment of Dsh, and therefore this also results in the loss of polarity (not shown). When Vang is removed from all cells in simulation, there is no mechanism to stabilize Dsh or Fz to a particular location in the cell, and so the remaining proteins tend to diffuse toward a uniform distribution. Only slight asymmetry in the distributions of Dsh and Fz is seen (not shown), resulting from the influence of the direct, global asymmetry signal. Such weak polarity in the model corresponds to a greater chance that hair polarity will be disrupted. It is interesting to try to reconcile why removing Pk in clones has only a very subtle phenotype, while a polarity defect is observed when Pk is removed from the whole tissue. In simulation, *pk* clones show reduced asymmetry in the distribution of Dsh (Figs. 2O,P,R of the main text, S7 and S13). In simulations in which Pk is removed from all cells, the asymmetry at the end of the simulation is even further degraded (not shown), making a disruption in the hair polarity more likely. This weak asymmetry would be very difficult to

detect experimentally, and is consistent with previous observations (*S41*). Pk function is therefore not redundant in the whole tissue, and one way to understand this is to consider that the robust polarization of wild-type cells surrounding a clone is sufficient to propagate polarity through a compromised *pk* null clone. As the clone size increases, the phenotype will approach that seen in whole mutant tissue.

Most previous experiments with Pk have used non-null alleles. As discussed extensively by Gubb (*S41*), one must postulate that the balance of activities of the Pk isoforms is important for function. In the clones producing domineering non-autonomy (and indeed a phenotype within the clone) the unbalanced influence of the isoforms on the function of the feedback loop must therefore produce these phenotypes. Since the nature of the non-null Pk isoforms is not understood, we have made no attempt to model them.

Materials and Methods

Cell Culture experiments were performed using 293T cells as described (*S21*). Proteins were expressed from the CS2 vector. 100 ng Fz, 100 ng Dsh::GFP, and 200 or 400 ng of Pk and Vang vectors were used, with empty CS2 to make a total of 1 μg. Transfections were performed in duplicate, and at least 500 cells were scored for predominantly cytoplasmic or membrane associated Dsh::GFP, with the viewer blinded to sample identity. Wing dissection, immunostaining and phalloidin staining were as described (*S21, S42*). Genotypes were:

fz^{R52} FRT2A/ubiGFP FRT2A; hs-FLP/+

y w dsh^{V26} f^{36a} FRT9-2/ubiGFP FRT9-2; T155GAL4 UAS-FLP/+

FRT42D $Vang^{A3}$/FRT42D ubiGFP; T155GAL4 UAS-FLP/+

FRT42D pk-$sple^{13}$/FRT42D ubiGFP; T155GAL4 UAS-FLP/+

dsh::GFP/+; fz^{X} where X=R52, F31 or J22 (ref. (*S12*)).

en-GAL4, UAS-pk/+; arm-fzEGFP8.9 (ref. (*S40*))

en-GAL4, UAS-pk/Dsh::GFP^{II}

hs-FLP/+; fz^{X} FRT2A/Act-Stbm-YFP where X=R52 or F31 (ref. (*S28*); Stbm is synonymous with Vang)

References

S1. G. Struhl, D. A. Barbash, P. A. Lawrence, *Development* **124**, 2155 (1997).

S2. M. Wehrli, A. Tomlinson, *Development* **125**, 1421 (1998).

S3. P. A. Lawrence, J. Casal, G. Struhl, *Development* **126**, 2441 (1999).

S4. P. N. Adler, J. Taylor, J. Charlton, *Mech Dev* **96**, 197 (2000).

S5. D. Strutt, R. Johnson, K. Cooper, S. Bray, *Curr Biol* **12**, 813 (2002).

S6. P. A. Lawrence, J. Casal, G. Struhl, *Development* **129**, 2749 (2002).

S7. P. N. Adler, *Developmental Cell* **2**, 525 (2002).

S8. M. Fanto, *et al.*, *Development* **130**, 763 (2003).

S9. M. P. Zeidler, N. Perrimon, D. I. Strutt, *Genes Dev* **13**, 1342 (1999).

S10. D. Gubb, A. Garcia-Bellido, *J Embryol Exp Morphol* **68**, 37 (1982).

S11. C. R. Vinson, P. N. Adler, *Nature* **329**, 549 (1987).

S12. K. H. Jones, J. Liu, P. N. Adler, *Genetics* **142**, 205 (1996).

S13. R. E. Krasnow, L. L. Wong, P. N. Adler, *Development* **121**, 4095 (1995).

S14. J. Klingensmith, R. Nusse, N. Perrimon, *Genes Dev* **8**, 118 (1994).

S15. H. Theisen, *et al.*, *Development* **120**, 347 (1994).

S16. R. E. Krasnow, P. N. Adler, *Development* **120**, 1883 (1994).

S17. J. Taylor, N. Abramova, J. Charlton, P. N. Adler, *Genetics* **150**, 199 (1998).

S18. J. Chae, *et al.*, *Development* **126**, 5421 (1999).

S19. H. Strutt, D. Strutt, *Developmental Cell* **3**, 851 (2002).

S20. C. Hirsch, *Numerical Computation of Internal and External Flows, Vol 1: Fundamentals of Numerical Discretization* (John Wiley & Sons, New York, NY, 1988).

S21. D. R. Tree, *et al.*, *Cell* **109**, 371 (2002).

S22. J. A. Nelder, R. Mead, *Computer Journal* **7**, 308 (1965).

S23. D. Blount, *The Annals of Probability* **19**, 1440 (1991).

S24. D. T. Gillespie, *J Phys Chem* **81**, 2340 (1977).

S25. H. H. McAdams, A. Arkin, *Proc Natl Acad Sci* **94**, 814 (1997).

S26. T. G. Kurtz, *J Chem Phys* **57**, 2976 (1972).

S27. R. Y. Tsien, *Annu Rev Biochem* **67**, 509 (1998).

S28. R. Bastock, H. Strutt, D. Strutt, *Development* **130**, 3007 (2003).

S29. A. Jenny, R. S. Darken, P. A. Wilson, M. Mlodzik, *Embo J* **22**, 4409 (2003).

S30. J. D. Axelrod, J. R. Miller, J. M. Shulman, R. T. Moon, N. Perrimon, *Genes Dev* **12**, 2610 (1998).

S31. J. D. Axelrod, *Genes Dev* **15**, 1182 (2001).

S32. T. Usui, *et al.*, *Cell* **98**, 585 (1999).

S33. F. Feiguin, M. Hannus, M. Mlodzik, S. Eaton, *Dev Cell* **1**, 93 (2001).

S34. G. Das, A. Jenny, T. J. Klein, S. Eaton, M. Mlodzik, *Development* **131**, 4467 (2004).

S35. M. Hannus, F. Feiguin, C.-P. Heisenberg, S. Eaton, *Development* **129**, 3493 (2002).

S36. F. Carreira-Barbosa, *et al.*, *Development* **130**, 4037 (2003).

S37. M. Takeuchi, *et al.*, *Curr Biol* **13**, 674 (2003).

S38. M. T. Veeman, D. C. Slusarski, A. Kaykas, S. H. Louie, R. T. Moon, *Curr Biol* **13**, 680 (2003).

S39. M. Park, R. T. Moon, *Nat Cell Biol* **4**, 20 (2002).

S40. D. I. Strutt, *Molecular Cell* **7**, 367 (2001).

S41. D. Gubb, *et al.*, *Genes Dev* **13**, 2315 (1999).

S42. Y. Shimada, T. Usui, S. ichi Yanagawa, M. Takeichi, T. Uemura, *Curr Biol* **11**, 859 (2001).

Table S1. Feature constraint functions representing the characteristic PCP phenotypes reproduced by the mathematical model.

Phenotype	**Objective**	**Constraint description**
Wild-type	J_{wt}	Asymmetric accumulation of Dsh and Fz on the distal cell membrane. Asymmetric accumulation of Pk and Vang on the proximal cell membrane (*S21, S28, S31, S40*).
dsh	$J_{\mathrm{d}sh}$	Polarity disruption inside of the mutant clone. Autonomous phenotype (*S14, S15*).
fz	$J_{\mathrm{f}z}$	Distal domineering non-autonomy (*S10*).
Vang	$J_{\mathrm{V}ang}$	Proximal domineering non-autonomy (*S17*).
pk	$J_{\mathrm{p}k}$	No polarity reversal. (this paper)
$>>dsh$	$J_{>>dsh}$	Proximal domineering non-autonomy. (our unpublished observations)
$>>fz$	$J_{>>fz}$	Proximal domineering non-autonomy (*S40*).
$>>Vang$	$J_{>>Vang}$	Distal domineering non-autonomy. (our unpublished observations)
$>>pk$	$J_{>>pk}$	Distal domineering non-autonomy.
$fz^{autonomous}$	$J_{\mathrm{f}za}$	Polarity disruption inside of the mutant clone. Autonomous phenotype (*S12*).
$>>fz^{autonomous}$	$J_{>>fza}$	Proximal domineering non-autonomy (*S40*).
EnGAL4, UASpk	$J_{>>pk-en}$	Overexpression of Pk results in protein accumulation to a degree greater than or equal to that for wild-type results (*S21*).

Table S2. Comparison of simulated and experimental protein localization. For loss-of-function and overexpression clones resulting from our parameter set using the reaction based asymmetry signal, we systematically compared the protein localization simulations to available experimental results. In nearly all cases, the simulations closely approximate the experimental results. The comparisons are tabulated as follows.

Clone	**Protein**	**Simulation**	**Experiment**	**Comment**
dsh	Dsh	Fig. S5.A	Ref. (*S42*)	
dsh	Fz	Fig. S5.B	Ref. (*S40*)	
fz	Dsh	Fig. S5.E	Ref. (*S42*)	
fz	Pk	Fig. S5.G	Ref. (*S21*)	
fz	Vang	Fig. S5.H	Ref. (*S28*)	
pk	Dsh	Fig. S5.I	Ref. (*S21*)	
pk	Fz	Fig. S5.J	Ref. (*S28*)	
pk	Pk	Fig. S5.K	Ref. (*S21*)	
pk	Vang	Fig. S5.L	Ref. (*S28*)	
Vang	Dsh	Fig. S5.M	Ref. (*S28*)	Staining quality was poor.
Vang	Fz	Fig. S5.N	Refs. (*S28, S40*)	
Vang	Pk	Fig. S5.O	Ref. (*S28*)	In the experimental result, some Pk remains associated with the membrane in the absence of Vang, most likely due to prenylation at its C-terminus. It is unclear whether this population of Pk contributes to inhibition of Dsh localization. No mechanism for membrane association in the absence of Vang was included in the simulation.
Vang	Vang	Fig. S5.P	Ref. (*S28*)	
$>>dsh$	Vang	Fig. S6.D	Ref. (*S28*)	The experimental result appears to show elevated levels of Vang inside the $>>dsh$ clone. Our simulations fix the total amount of protein.
$>>fz$	Fz	Fig. S6.F	Ref. (*S40*)	
$>>fz$	Vang	Fig. S6.H	Ref. (*S28*)	
$>>fz^{\text{autonomous}}$	Fz	Fig. S7.N	Ref. (*S40*)	
$>>pk$	Vang	Fig. S6.L	Ref. (*S28*)	The experimental result appears to show elevated levels of Vang inside the $>>pk$ clone. Our simulations fix the total amount of protein.
$>>Vang$	Fz	Fig. S6.N	Ref. (*S28*)	
$>>Vang$	Pk	Fig. S6.O	Ref. (*S28*)	Staining quality was poor.

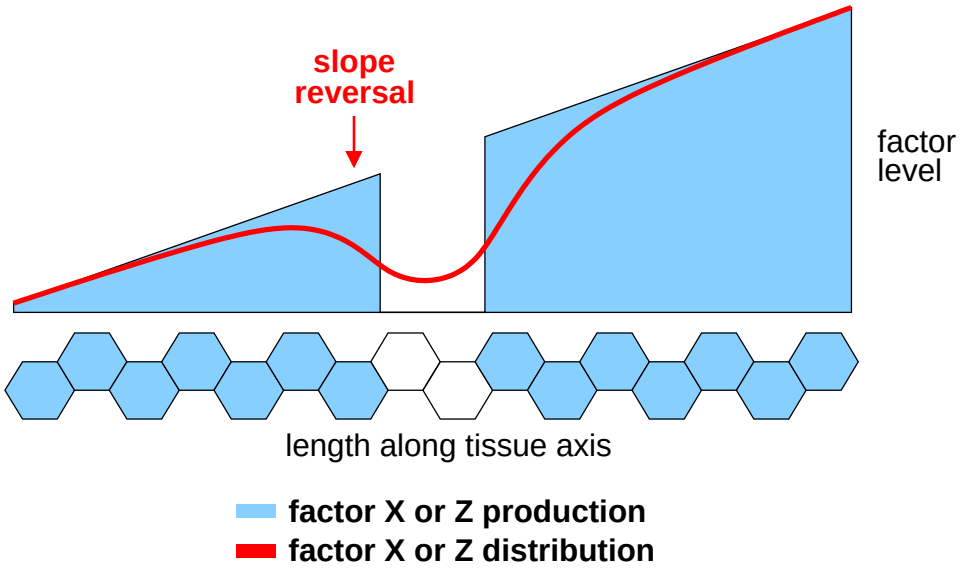

Figure S1. Diagram illustrating proposed PCP signaling models invoking a diffusible factor "X" or "Z." Domineering non-autonomy in regions around mutant clones in which production of the factor is suppressed (shown) or enhanced (not shown) would result from diffusion of the factor, followed by reading of the factor gradient.

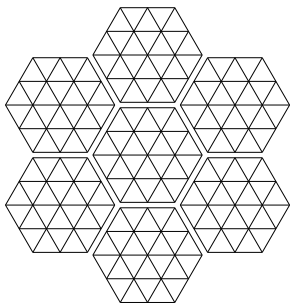

Figure S2. Computational grid showing the edge relationship between cells and an example triangular grid for each cell.

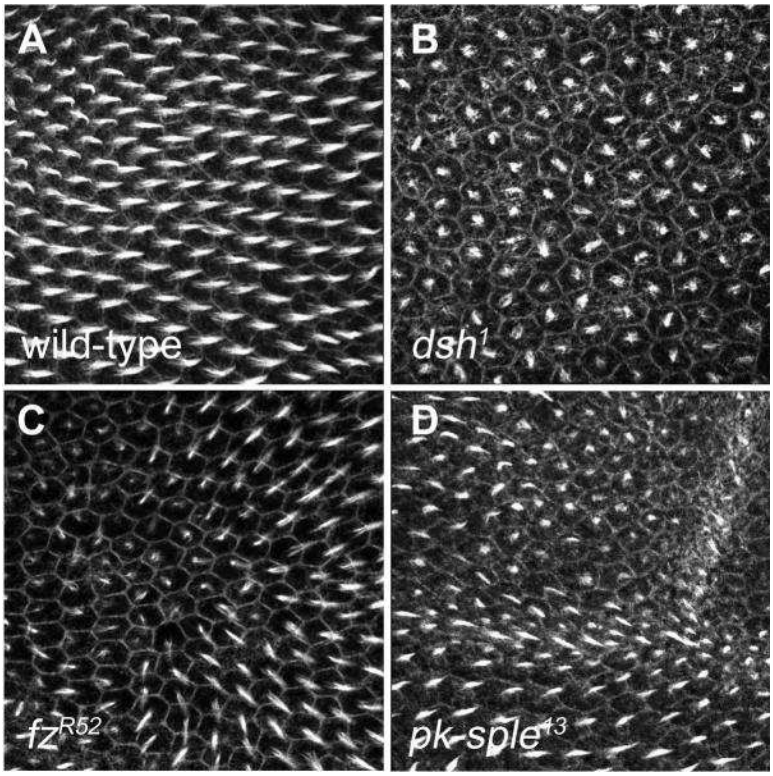

Figure S3. Phalloidin stained wings showing location of prehair emergence. Wild-type cells produce prehairs emerging from the distal vertex (A). In contrast fz^{R52} (C) *pk-sple*^{13} (D) and *Vang* (not shown) mutants produce many prehairs emerging from the center of the cell, though some emerge closer to or at the periphery. dsh^{1} (B) wings produce prehairs uniformly from the center of the cell. Prehair emergence is also delayed in *dsh* mutant cells to a greater extent than in the other mutants (see also the clones in Fig. 2 of the main paper).

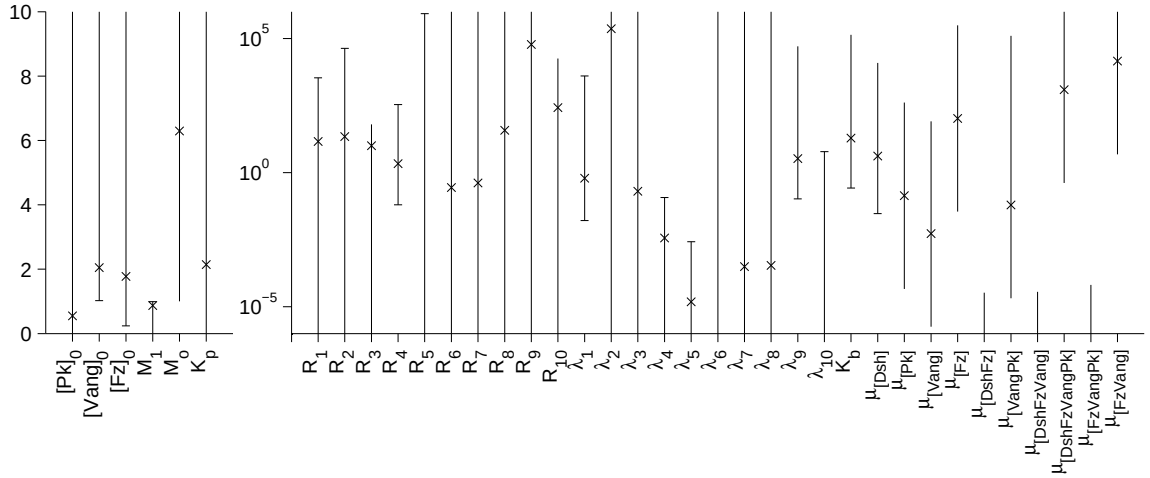

(A) J_{wt}

Figure S4. Ranges of parameters for which, when varied individually, each feature constraint is satisfied. $\times$ symbols mark the selected parameter values used in producing our simulation results. Uncapped lines indicate that a limit was not found because a search limit was reached before the constraint was violated. The search limits for the diffusion constants were smaller than for other parameters because extreme values of diffusion constants substantially slow down the numerical simulation.

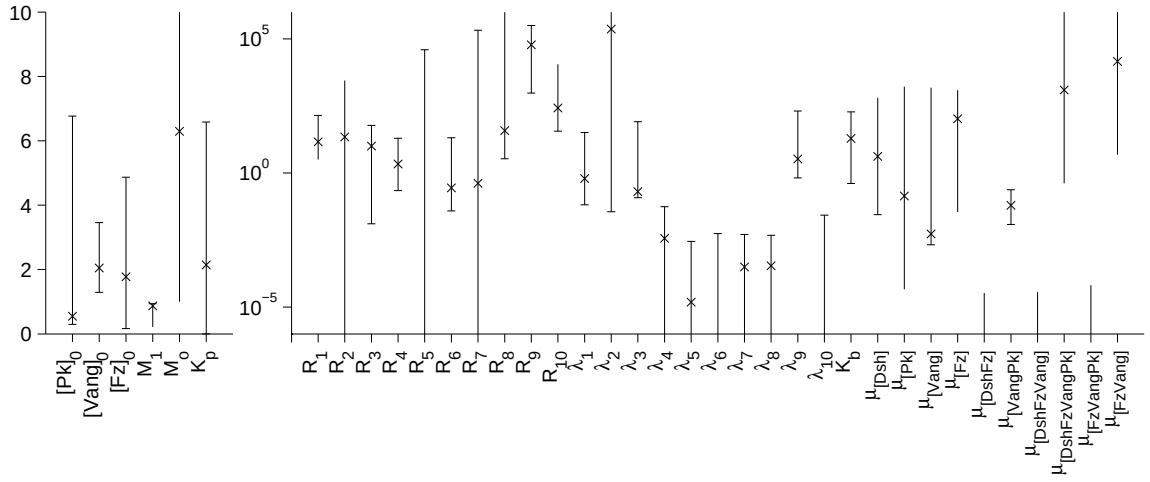

(B) J_{dsh}

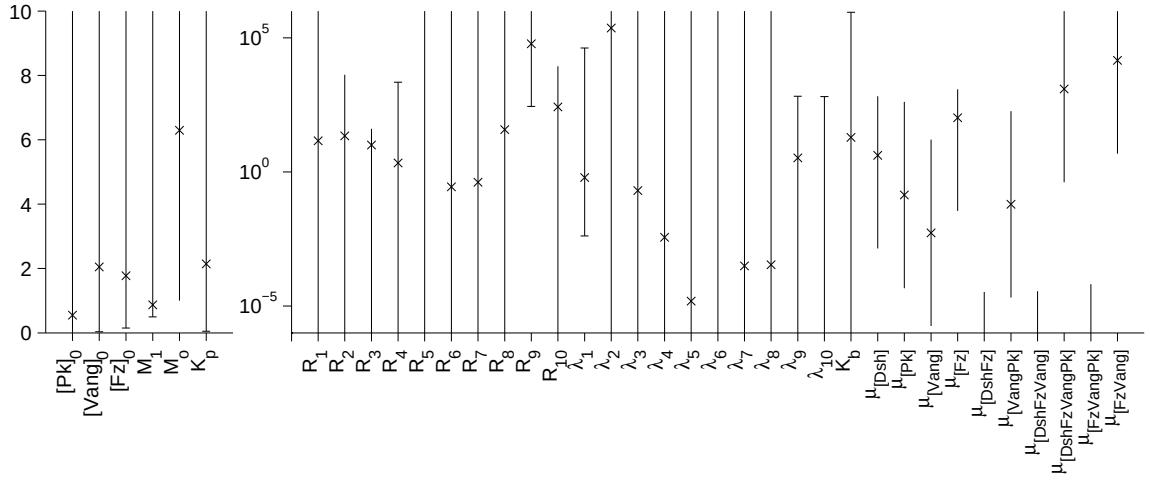

(C) J_{fz}

Figure S4. continued.

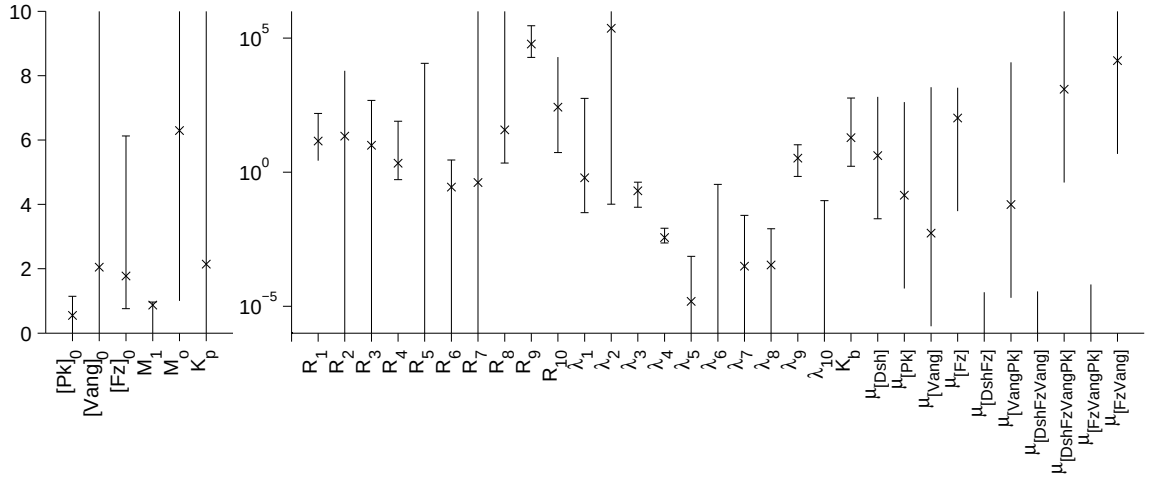

(D) J_{pk}

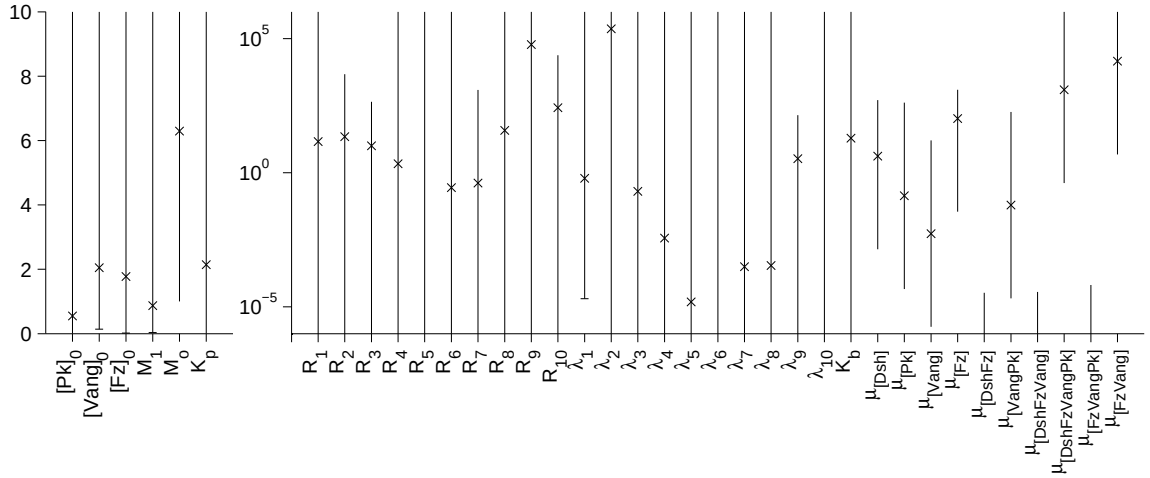

(E) J_{Vang}

Figure S4. continued.

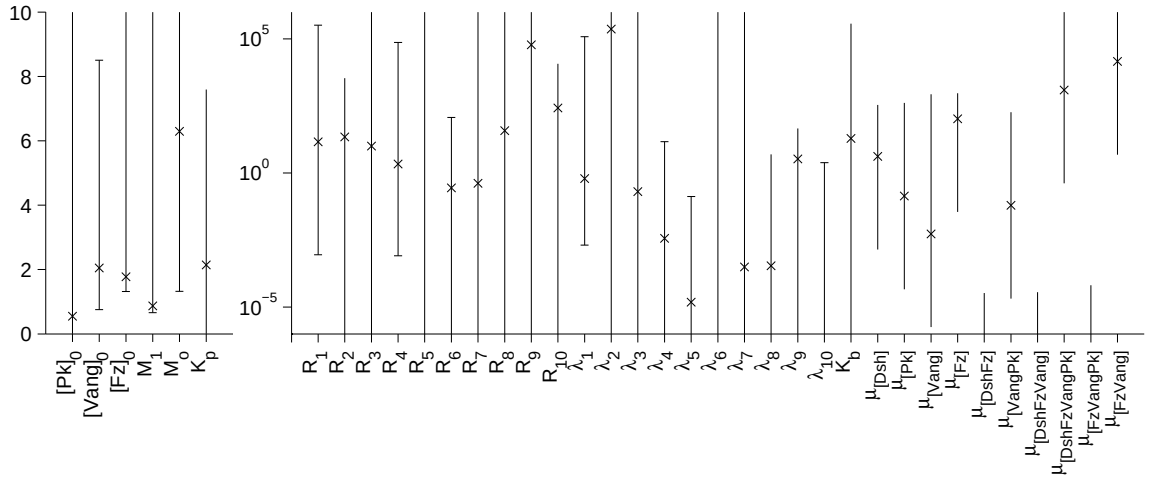

(F) $J_{>>\mathrm{dsh}}$

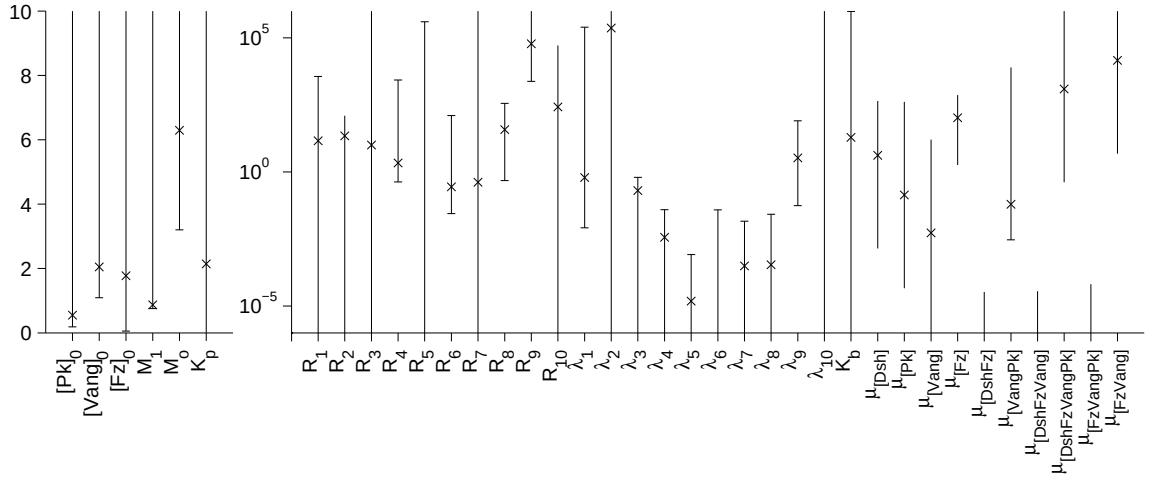

(G) $J_{>>\mathrm{fz}}$

Figure S4. continued.

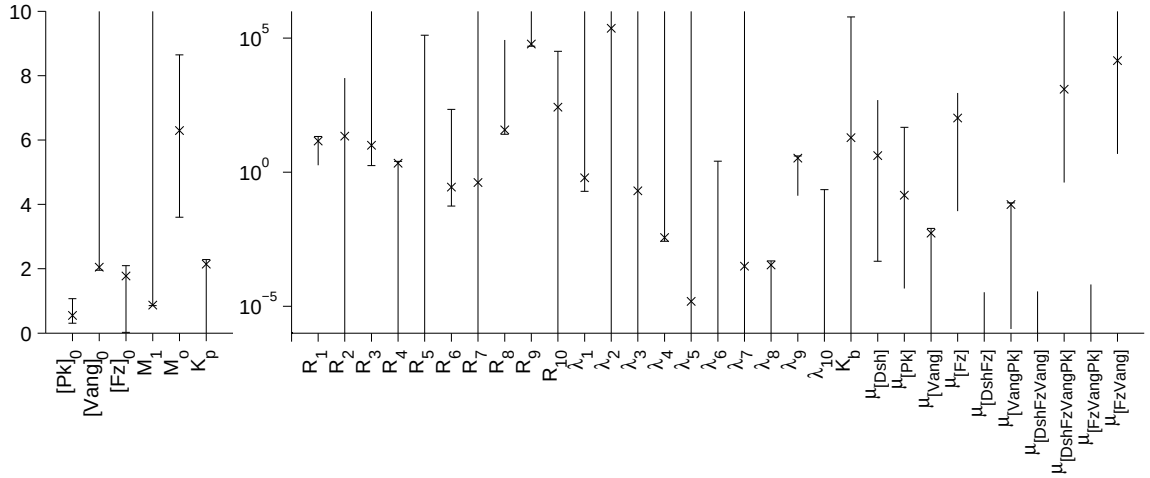

(H) $J_{>>\mathrm{pk}}$

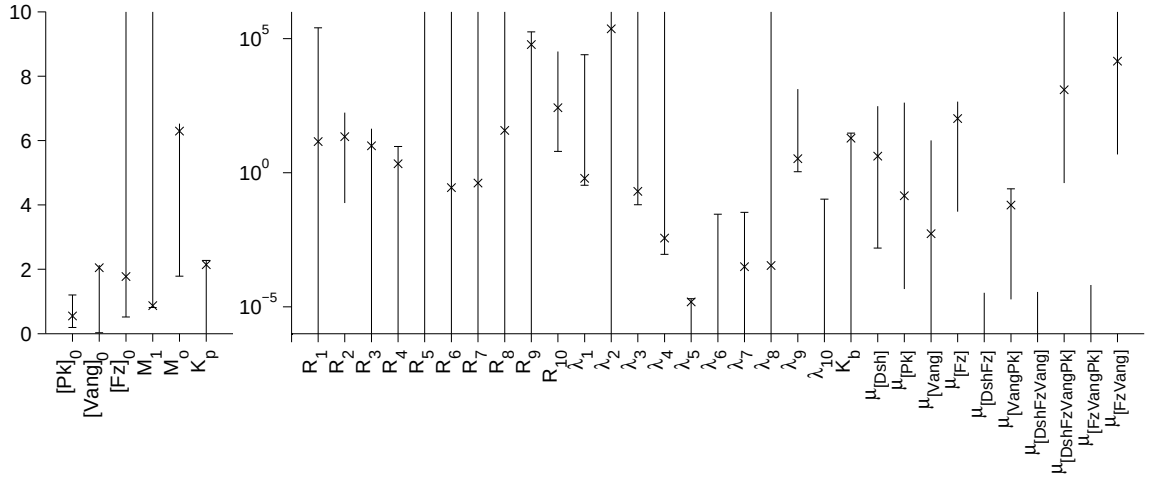

(I) $J_{>>\mathrm{Vang}}$

Figure S4. continued.

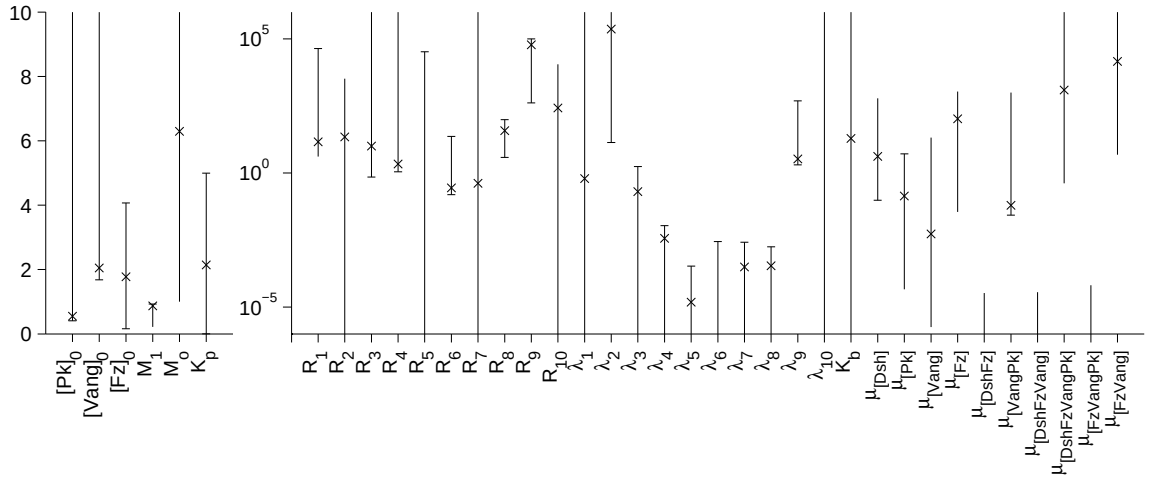

(J) J_{fza}

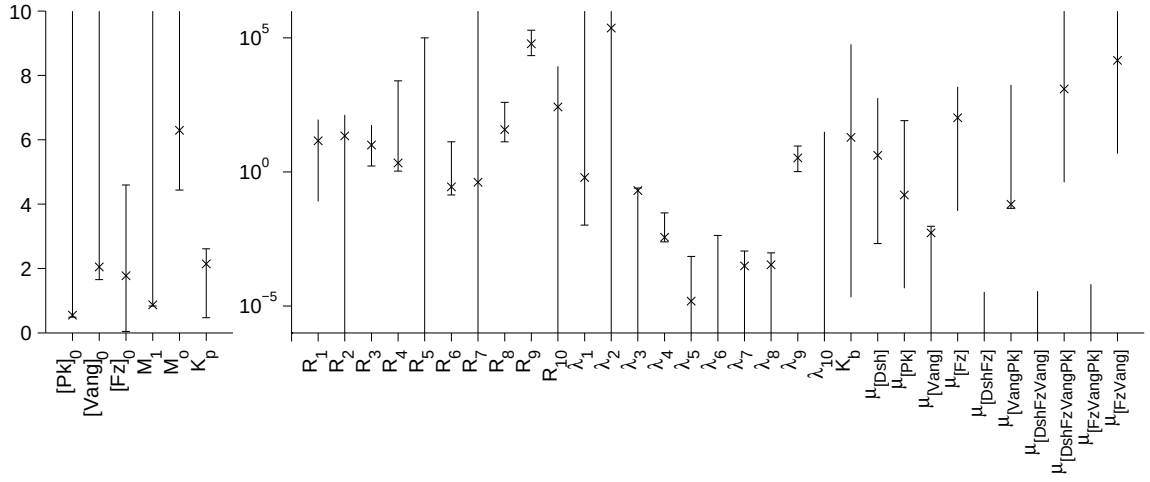

(K) $J_{>>\mathrm{fza}}$

Figure S4. continued.

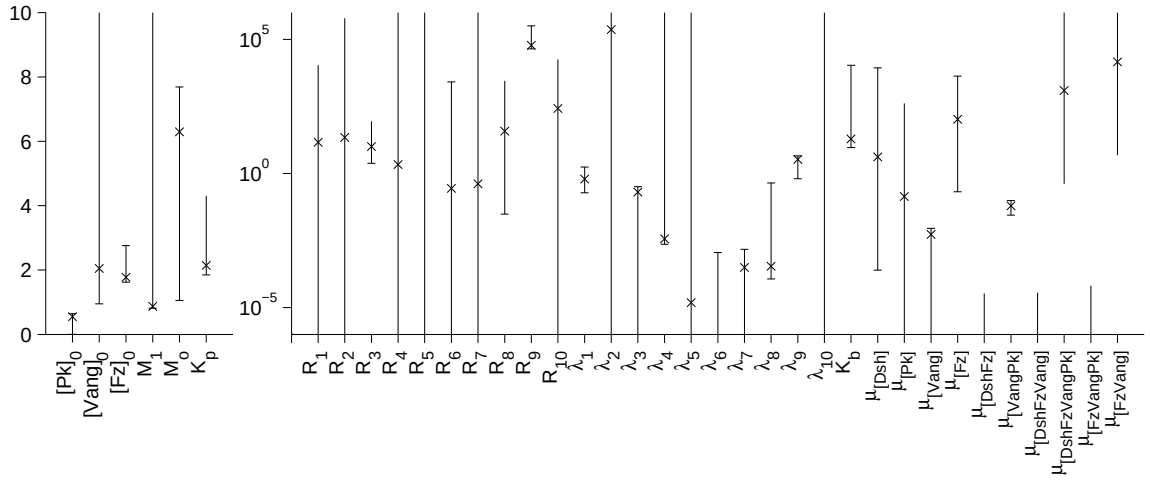

(L) $J_{\mathrm{pk-en}}$

Figure S4. continued.

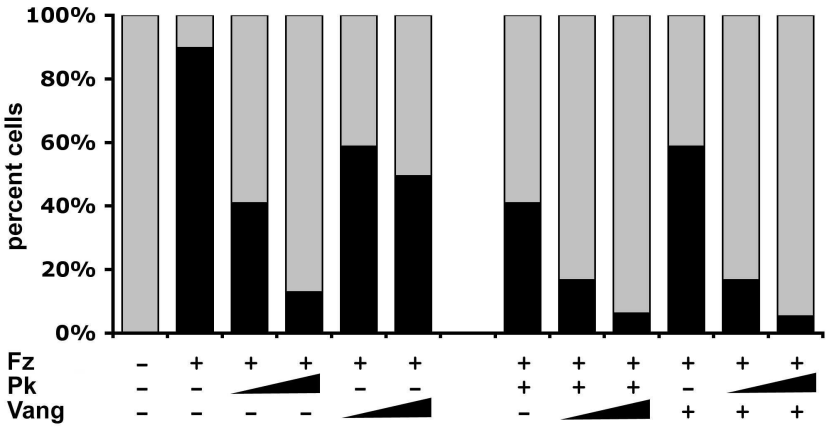

Figure S5. Dose response to Pk and Vang showing inhibition of Dsh recruitment to the membrane. Cells were transfected with Dsh::GFP and the indicated additional proteins; the % of cells with predominantly cytoplasmic (gray) or membrane associated (black) Dsh::GFP are shown. Wedges indicate increasing doses of Pk or Vang (200 or 400 ng), and pluses indicate 200 ng of Pk or Vang, or 100 ng of Fz. Pk and Vang each show a dose dependent inhibition of Dsh::GFP membrane association, and the effect is enhanced when expressed together. The same doses of LacZ had no significant effect on Fz dependent Dsh::GFP localization (not shown).

Figure S6. Diagrams illustrating possible mechanisms for a direct, global asymmetry signal. The asymmetric distribution or activation of the input signal results in a change along the length of the tissue axis in the response of the feedback loop, such as a difference in the reaction rates or diffusion rates of the model. (A) A factor is asymmetrically distributed or activated prior to the asymmetric localization of the modeled proteins. For example, Wdb is asymmetrically arrayed in cells preceding the observed asymmetry of Fz, Dsh, Vang and Pk. (B) The asymmetry signal represents an expression gradient. The directional bias results from the differences in the relative response of a cell with neighboring cells. (C) The network responds directly to a globally imposed gradient. This asymmetry signal can be decomposed into an asymmetry resulting from differences in the relative response of a cell with neighboring cells as in (B), and from the difference in response between the proximal and distal edge of each cell. (D) For this second component of the asymmetry from (C), if the gradient is taken to be shallow such that differences between neighboring cells can be neglected, then the asymmetry seen by cells can be taken to be locally identical, but would vary more significantly between the proximal and distal regions of the cell array.

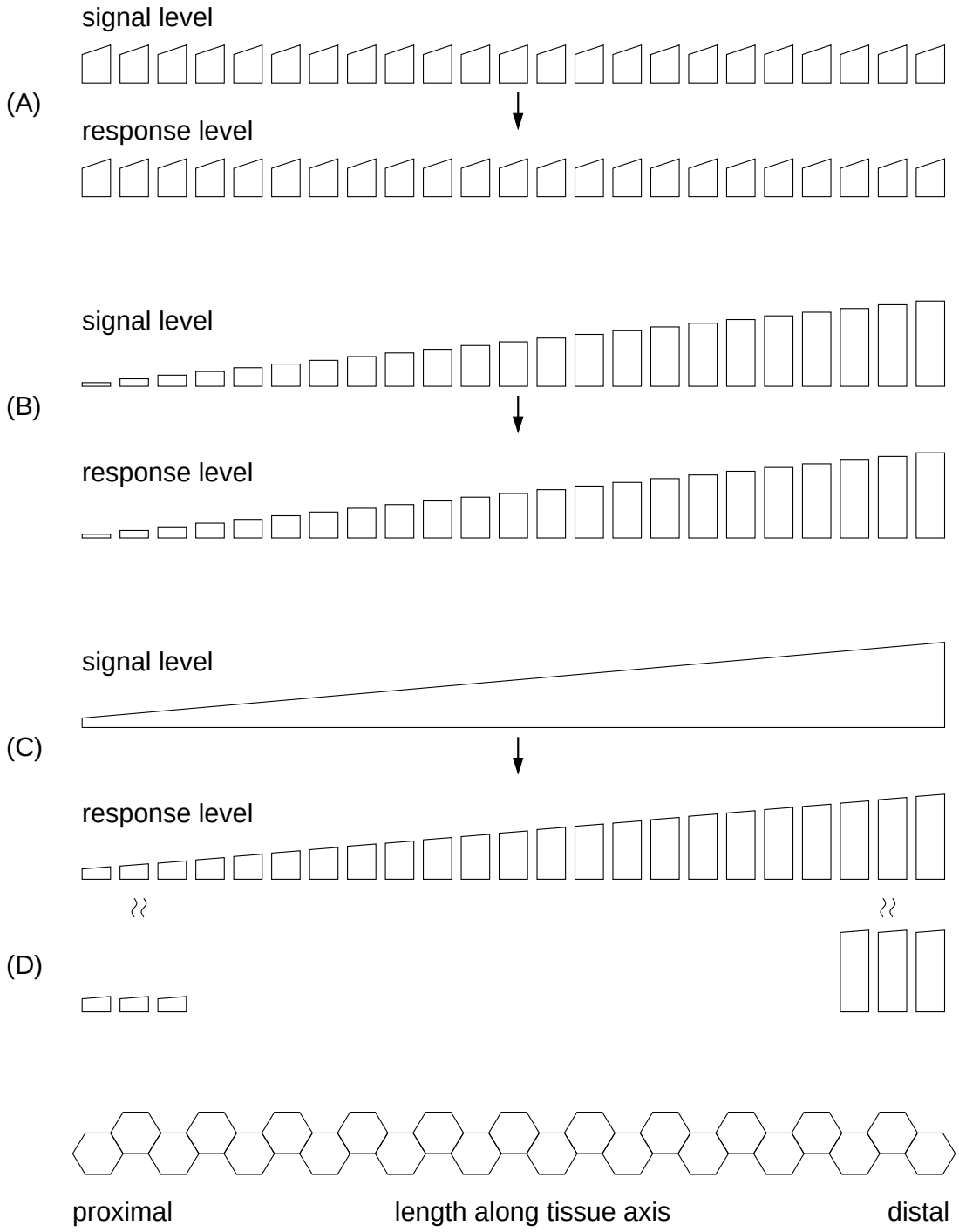
signal level
(A)
response level
signal level
(B)
response level
signal level
(C)
response level
(D)
proximal
length along tissue axis
distal

Figure S6.

Figure S7. Simulation results obtained from the parameter set using the reaction-based asymmetry signal showing clones of cells mutant for *dsh* (A-D), *fz* (E-H), *pk* (I-L) and *Vang* (M-P). Shown are the distributions of Dsh (A, E, I and M), Fz (B, F, J and N), Pk (C, G, K and O) and Vang (D, H, L and P). Simulations were performed on a 20×32 periodic array of cells.

Figure S8. Simulation results obtained from the parameter set using the reaction-based asymmetry signal showing clones of cells with 6.29× overexpression of *dsh* (A-D), *fz* (E-H), *pk* (I-L) and *Vang* (M-P). Shown are the distributions of Dsh (A, E, I and M), Fz (B, F, J and N), Pk (C, G, K and O) and Vang (D, H, L and P). Simulations were performed on a 20×32 periodic array of cells.

Figure S9. Simulation results obtained from the parameter set using the reaction-based asymmetry signal showing $fz^{\text{autonomous}}$ clones. The interaction of Fz with Vang is left intact, while the reaction rates of Fz with Dsh have been reduced to 0% (A-D), 0.01% (E-H) and 0.02% (I-L). Panels M-P show the effect of 6.29× overexpression of $\text{Fz}^{\text{autonomous}}$with 0.01% of the Fz-Dsh interaction. Shown are the distributions of Dsh (A, E, I and M), Fz (B, F, J and N), Pk (C, G, K and O) and Vang (D, H, L and P). Simulations were performed on a 20×32 periodic array of cells.

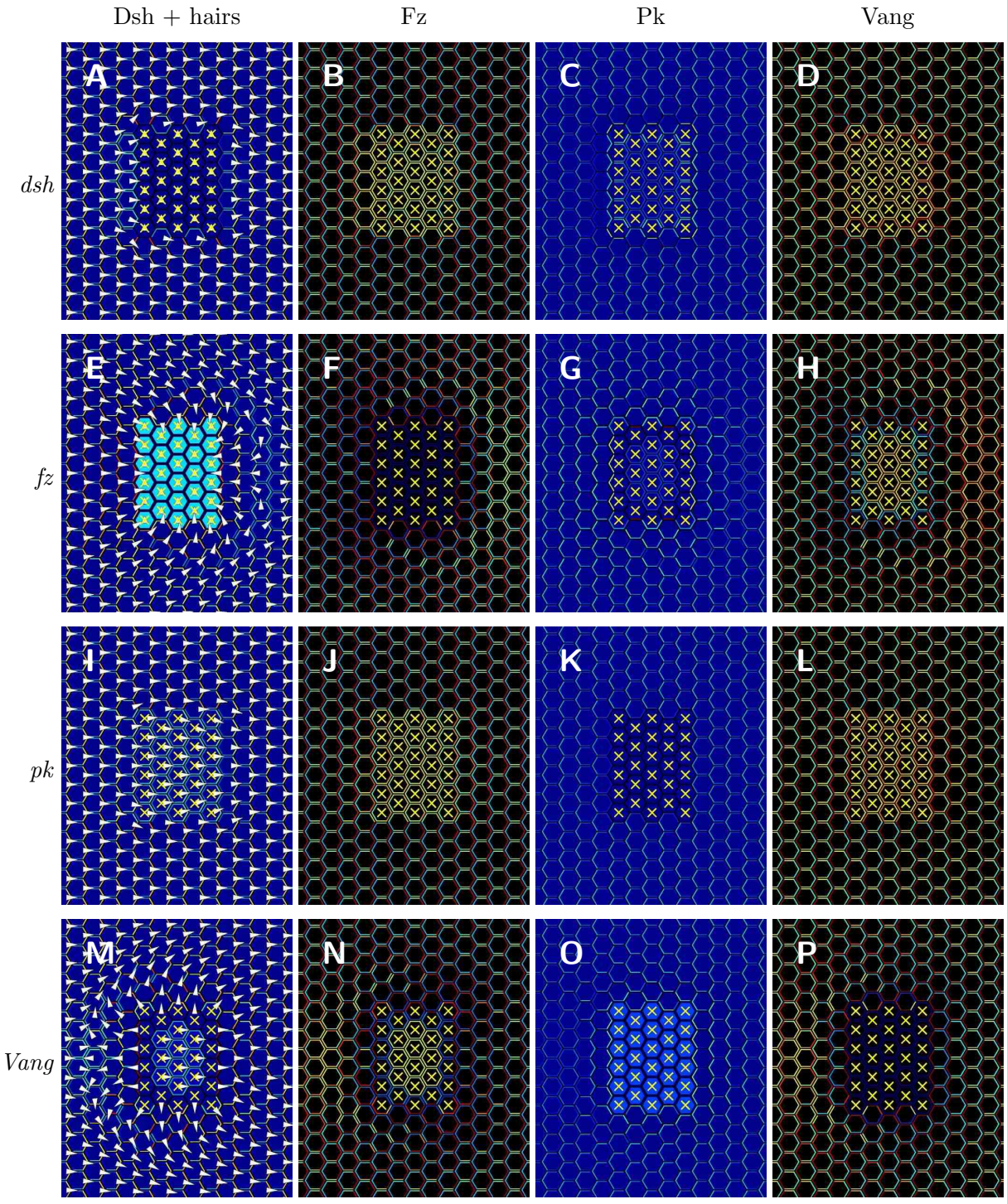

Figure S7.

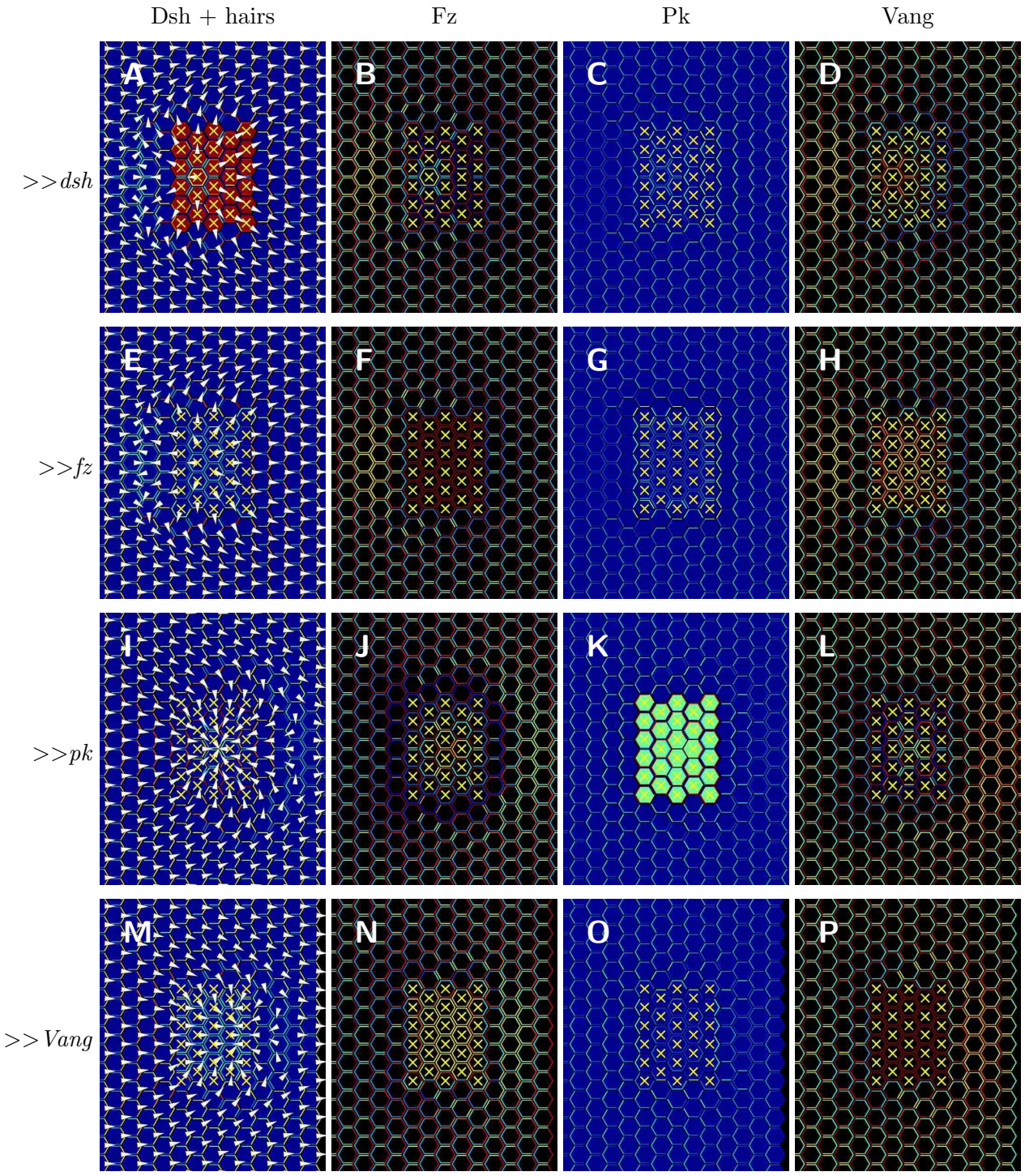

Figure S8.

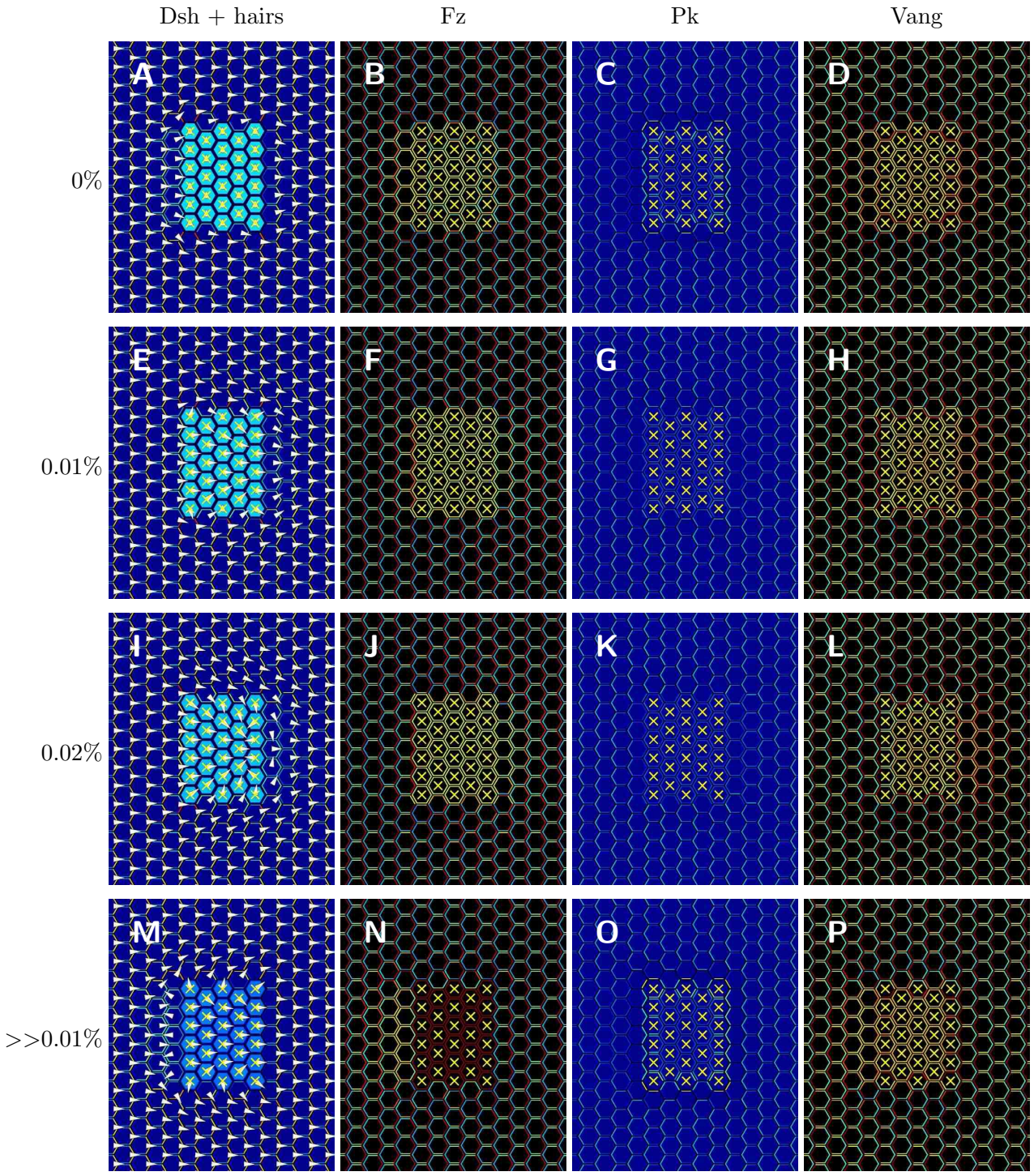

Figure S9.

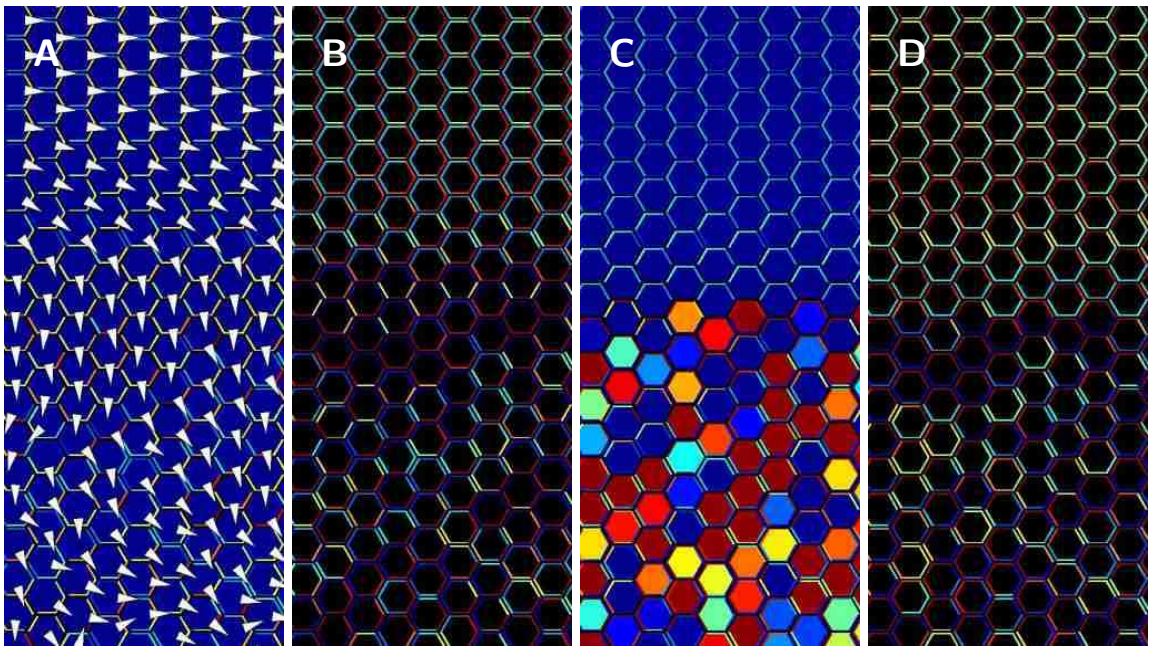

Figure S10. Simulation results obtained from the parameter set using the reaction-based asymmetry signal for a periodic 10×80 array of cells, in which *pk* was variably overexpressed from 1× to 11.58× within a band aligned with the proximal-distal axis and extending 40 cells along the anterior-posterior axis (as in Fig. 3 of the main text). Shown are the concentration distributions of Dsh (A), Fz (B), Pk (C) and Vang (D).

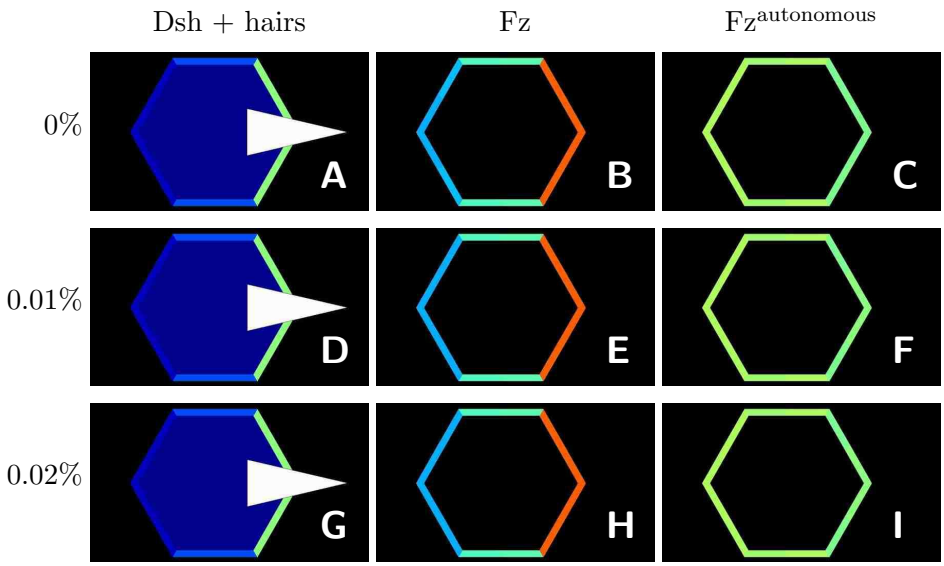

Figure S11. Simulation results in which *fz*$^{\text{autonomous}}$ is expressed in a wild-type background, with an initial concentration of 10% that of the wild-type Fz concentration. The interaction of Fz$^{\text{autonomous}}$ with Vang is left intact, while the reaction rates of Fz$^{\text{autonomous}}$ with Dsh have been reduced to 0% (A-C), 0.01% (D-F) and 0.02% (G-I). Shown are the distributions of Dsh (A, D and G), Fz (B, E and H) and Fz$^{\text{autonomous}}$ (C, F and I). The color scale for Fz$^{\text{autonomous}}$ (C, F and I) has been compressed by a factor of 10 so that a comparison between the relative amount of asymmetric localization could be made with that of the wild-type Fz (B, E and H).

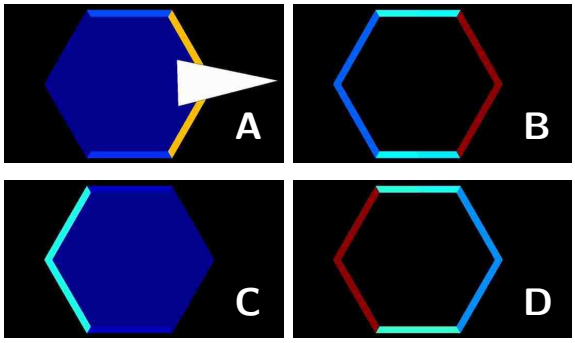

Figure S12. Wild-type simulation results showing the concentration distributions of Dsh (A), Fz (B), Pk (C) and Vang (D) corresponding to Fig. 2A-D of the main paper, but obtained from the parameter set using the diffusion-based asymmetry signal.

Figure S13. Simulation results obtained from the parameter set using the diffusion-based asymmetry signal showing clones of cells mutant for *dsh* (A-D), *fz* (E-H), *pk* (I-L) and *Vang* (M-P). Shown are the distributions of Dsh (A, E, I and M), Fz (B, F, J and N), Pk (C, G, K and O) and Vang (D, H, L and P). Simulations were performed on a 20×32 periodic array of cells. Compare with Fig. S7.

Figure S14. Simulation results obtained from the parameter set using the diffusion-based asymmetry signal showing clones of cells with 4.47× overexpression of *dsh* (A-D), *fz* (E-H), *pk* (I-L) and *Vang* (M-P). Shown are the distributions of Dsh (A, E, I and M), Fz (B, F, J and N), Pk (C, G, K and O) and Vang (D, H, L and P). Simulations were performed on a 20×32 periodic array of cells. Compare with Fig. S8.

Figure S15. Simulation results obtained from the parameter set using the diffusion-based asymmetry signal showing $fz^{\text{autonomous}}$ clones. The interaction of Fz with Vang is left intact, while the reaction rates of Fz with Dsh have been reduced to 0% (A-D), 0.01% (E-H) and 0.02% (I-L). Panels M-P show the effect of 4.47× overexpression of $\text{Fz}^{\text{autonomous}}$with 0.01% of the Fz-Dsh interaction. Shown are the distributions of Dsh (A, E, I and M), Fz (B, F, J and N), Pk (C, G, K and O) and Vang (D, H, L and P). Simulations were performed on a 20×32 periodic array of cells. Compare with Fig. S9.

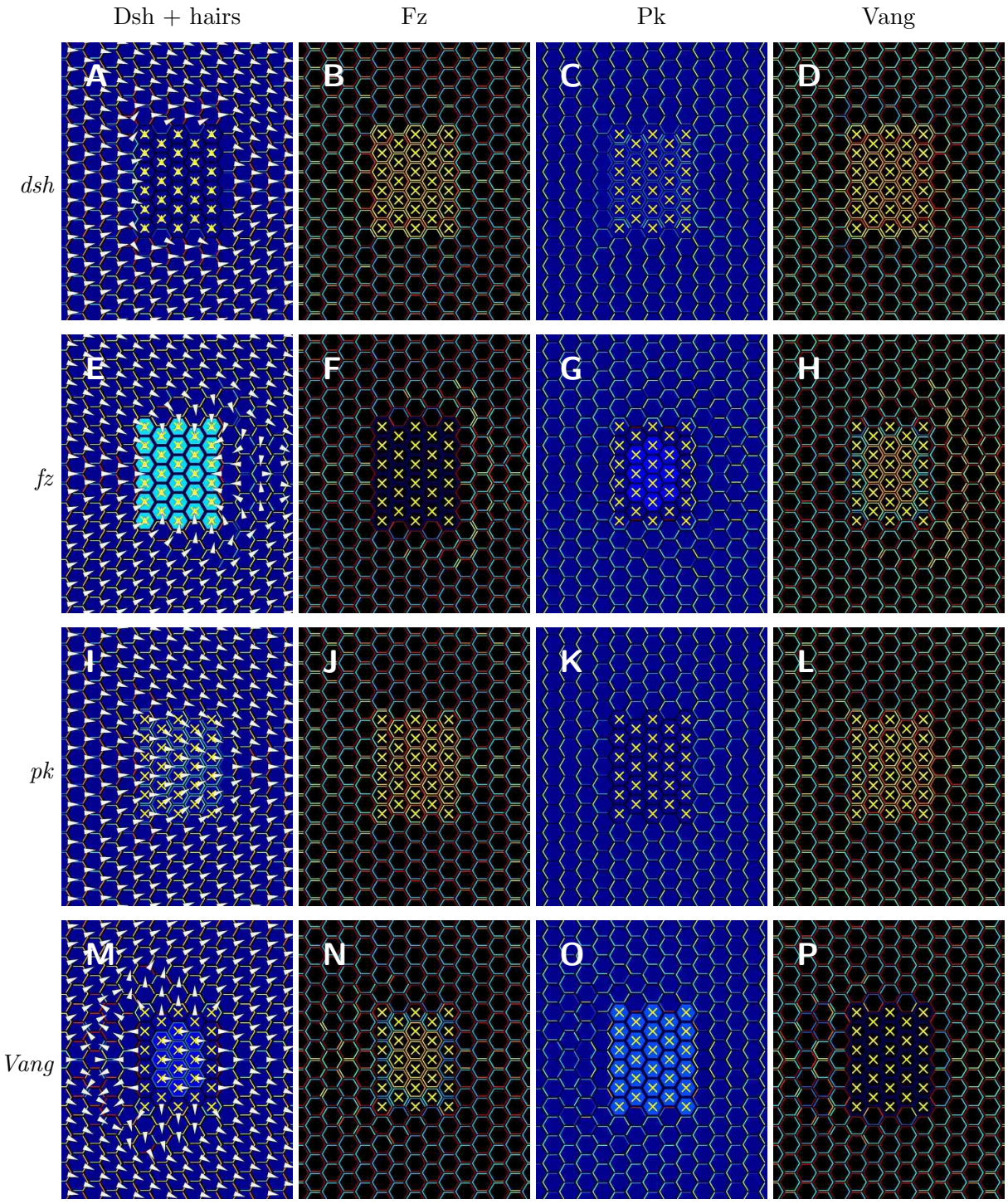

Figure S13.

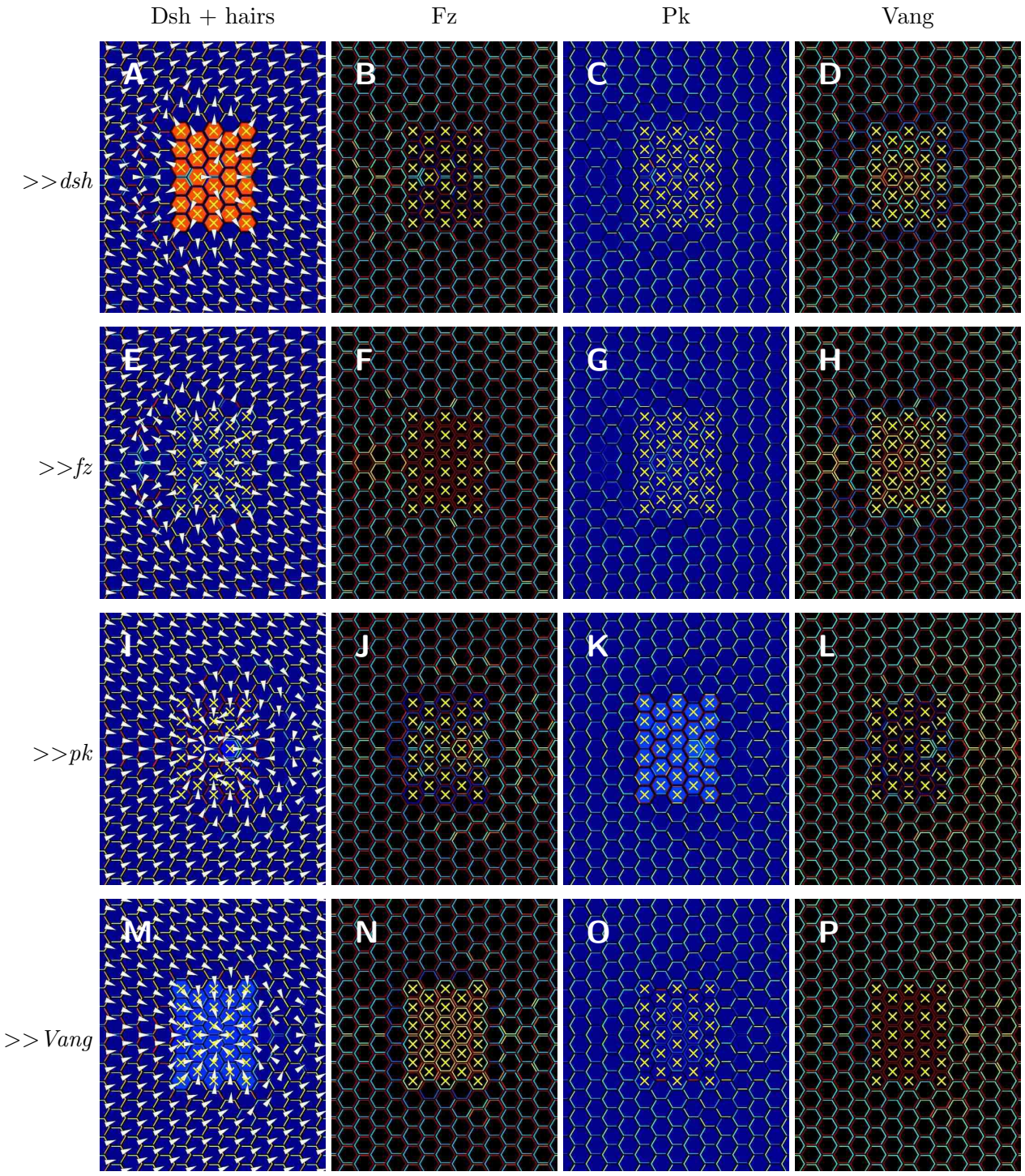

Figure S14.

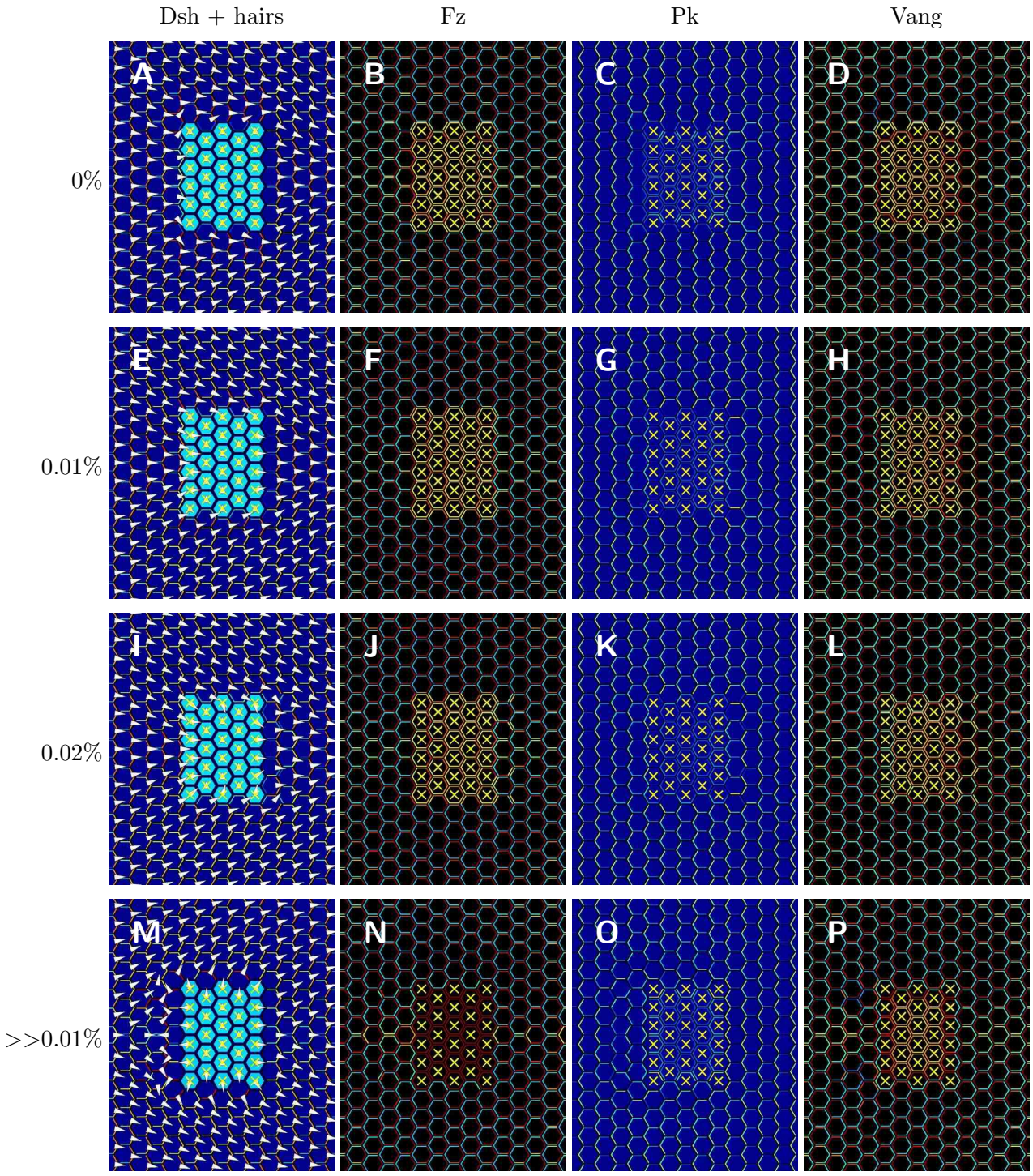

Figure S15.

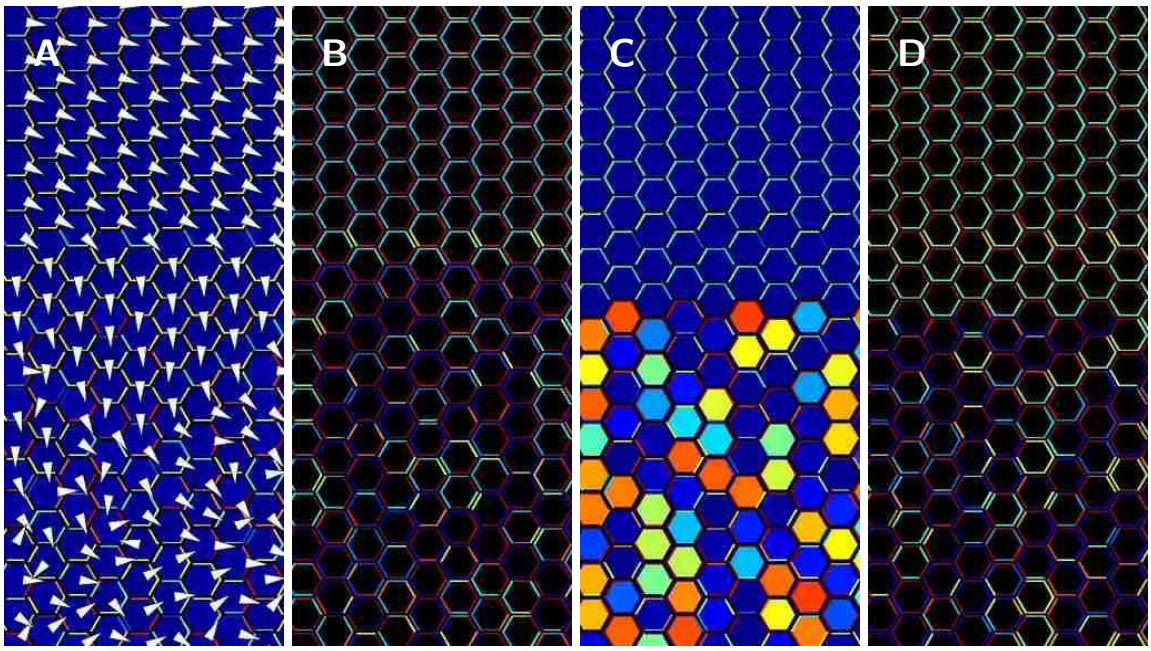

Figure S16. Simulation results obtained from the parameter set using the diffusion-based asymmetry signal for a periodic 10×80 array of cells, in which *pk* was variably overexpressed from 1× to 7.94× within a band aligned with the proximal-distal axis and extending 40 cells along the anterior-posterior axis (as in Fig. 3 of the main text). Shown are the concentration distributions of Dsh (A), Fz (B), Pk (C) and Vang (D). Compare with Fig. S10.